



Mathematical modelling of stretch-induced membrane traffic in bladder umbrella cells



D.E. Moulton^{a,*}, V. Sulzer^a, G. Apodaca^b, H.M. Byrne^a, S.L. Waters^a

^a Mathematical Institute, University of Oxford, Oxford, UK

^b Departments of Medicine and Cell Biology, University of Pittsburgh, USA

HIGHLIGHTS

- Multiscale model developed for vesicle traffic in response to mechanical stimuli.
- Explanation for counterintuitive non-monotonic behaviour observed in experiments.
- *In vivo* modelling uncovers potential root of bladder disorders in vesicle machinery.
- Clinical potential demonstrated with extensions to mechanical role in innervation.

ARTICLE INFO

Article history:

Received 19 November 2015

Received in revised form

21 March 2016

Accepted 24 August 2016

Available online 31 August 2016

Keywords:

Exocytosis

Endocytosis

Mechanosensing

Uroepithelium

ABSTRACT

The bladder is a complex organ that is highly adaptive to its mechanical environment. The umbrella cells in the bladder uroepithelium are of particular interest: these cells actively change their surface area through exo- and endocytosis of cytoplasmic vesicles, and likely form a critical component in the mechanosensing process that communicates the sense of ‘fullness’ to the nervous system. In this paper we develop a first mechanical model for vesicle trafficking in umbrella cells in response to membrane tension during bladder filling. Recent experiments conducted on a disc of uroepithelial tissue motivate our model development. These experiments subject bladder tissue to fixed pressure differences and exhibit counterintuitive area changes. Through analysis of the mathematical model and comparison with experimental data in this setup, we gain an intuitive understanding of the biophysical processes involved and calibrate the vesicle trafficking rate parameters in our model. We then adapt the model to simulate *in vivo* bladder filling and investigate the potential effect of abnormalities in the vesicle trafficking machinery on bladder pathologies.

© 2016 Elsevier Ltd. All rights reserved.

1. Introduction

Epithelial cells are continuously exposed to mechanical forces (e.g., stretch, compression, and shear stress), which affect all aspects of their biology. For example, inhaling air into the lungs stimulates surfactant release (Hildebran et al., 1981), shear stress and increased wall tension cause endothelial cells to release endothelin (Burnstock, 1999), and bladder filling stimulates the exocytosis of subapical Discoidal- and/or Fusiform-shaped Vesicles (DFVs) in umbrella cells, dramatically increasing their apical surface area (Apodaca, 2003; Truschel et al., 2002). Despite our understanding of the importance and physiological regulation of these events, we have limited insights into how mechanical forces affect these trafficking events. To gain insight into the complex

interactions between epithelial cells and mechanical forces, in this paper we develop a mathematical model specifically aimed at understanding bladder epithelium.

The primary function of the mammalian bladder is the temporary storage of urine collected from the kidneys. The bladder must accommodate large changes in volume while maintaining strong impermeability. The bladder urothelium is comprised of three layers: basal cells (~10 μm in diameter) form a single layer, intermediate cells (10–25 μm in diameter) are from one to several cell layers thick, and the large (25–250 μm in diameter) polyhedral umbrella cells form a single layer on the lumen side of the bladder wall (see Fig. 1). While the basal and intermediate cells may slide past one another during bladder filling, the umbrella cells undergo key morphological changes (Lewis, 2000) and form the focus of this study.

The general understanding of the activities of the bladder urothelium during filling and voiding has changed significantly over recent decades. In early literature, the large changes in volume and

* Corresponding author.

E-mail address: moulton@maths.ox.ac.uk (D.E. Moulton).

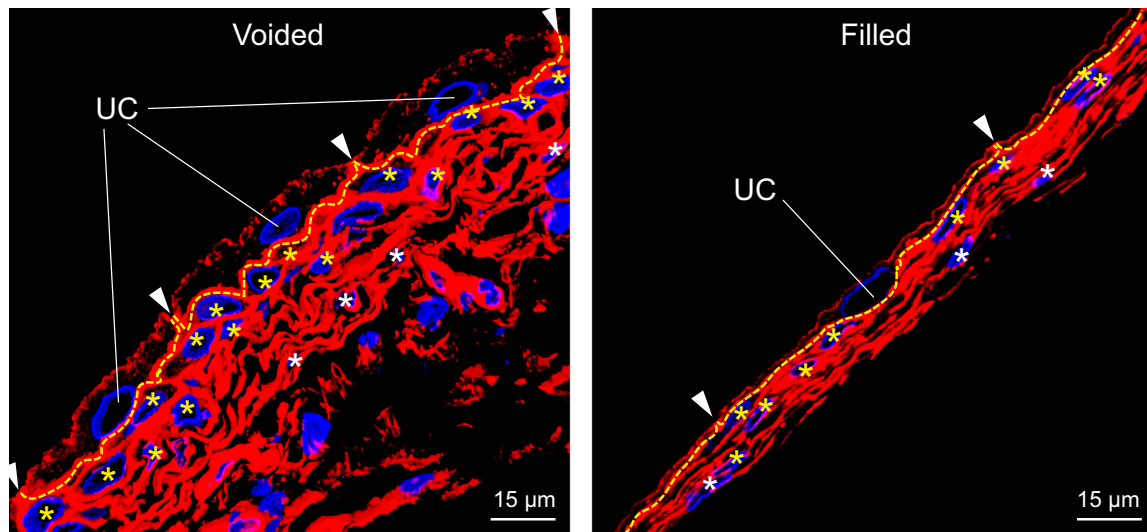


Fig. 1. Bladder urothelium in voided and filled bladder. The basolateral surface of the umbrella cells (UC) are marked by the yellow dashed line and the position of the tight junctions are indicated with arrowheads. Intermediate cells are marked with yellow asterisks, and basal cells with white asterisks. Reproduced with permission (Carattino et al., 2013). (For interpretation of the references to color in this figure, the reader is referred to the web version of this article.)

pressure were thought to be accommodated solely by unfolding of the highly wrinkled apical membrane of umbrella cells (Lewis, 2000; Staehelin et al., 1972). There has since been mounting evidence that vesicle trafficking in the umbrella cells plays a key role as well. Several experimental studies found that exocytosis of cytoplasmic vesicles in the apical membrane occurs in response to mechanical stimuli (Lewis and de Moura, 1982; Wang et al., 2003). In exocytosis, vesicles fuse with the membrane wall, increasing the surface area and thus relieving mechanical stress and facilitating an increase in bladder volume. This understanding has since been revised, as it was found that both exocytosis and endocytosis in the apical membrane occur simultaneously (Truschel et al., 2002), with endocytosis¹ thought to be modulating the change in surface area.

Numerous *in vitro* experimental investigations have been performed to understand vesicle trafficking and mechanotransduction in umbrella cells (Wang et al., 2003; Truschel et al., 2002; Soldati and Schliwa, 2006; Lewis and de Moura, 1982; Lewis and De Moura, 1984; Apodaca, 2002). Of particular interest is the recent work of Yu et al. (2009), in which it was demonstrated that stretch, and not pressure, is the mechanical stimulus that induces exo- and endocytosis in umbrella cell tissues. Evidence was also found suggesting a feedback relationship in vesicle traffic between the basal and apical membranes of the umbrella cells and that tension in the basal membrane might trigger endocytosis in the apical side. This work also demonstrated an intriguing non-monotonic behaviour in the apical surface area during the so-called “early stage” of bladder filling: when subjected to a pressure difference across the epithelial tissue, the apical membrane showed a rapid increase in surface area on the time scale of the first minute, followed by a decrease in surface area over the next several minutes, and finally a slow increase in surface area over the course of an hour. While exo- and endocytosis are well confirmed on the apical membrane of umbrella cells and clearly triggered by mechanical events (Truschel et al., 2002), it is less clear whether similar vesicle traffic occurs on the basal membrane. Though mechanisms for vesicle insertion have been proposed for both membranes (Alroy and Weinstein, 1980), the basal membrane does not seem to undergo significant exo- and endocytosis, at least

on long time-scale filling events (Truschel et al., 2002).

These experimental results highlight the importance of both mechanics and geometry in the urothelium. As the bladder fills, mechanical stimuli trigger unfolding and/or vesicle trafficking, each of which is effectively a change in geometry. This mechanically driven change can serve several important functions. An increase in apical surface area enables the bladder to accommodate an increasing volume; it also helps alleviate rising pressure, which may be needed for surface cells to maintain their barrier function. Moreover, the change in geometry feeds back to alter the stress levels in the bladder wall.

Along with volume accommodation and barrier function, of equal importance in a healthy bladder is communication with the brain. As with the morphological changes discussed above, the understanding of the urothelium’s role in this process has changed over time. Initially thought of as a passive barrier, the urothelium is now seen as an active sensory organ (Birder et al., 2010). Urothelial cells sense and transduce information about physical stimuli (Korossis et al., 2006; Birder et al., 2009), make intimate connections with afferent nerves (Iggo, 1955; Birder et al., 2009), and can directly alter the activities of the underlying detrusor muscle (Birder et al., 2012). The bladder operates through a bi-directional signalling process, whereby the bladder wall must communicate the sense of “fullness” to the brain prior to the bladder reaching full volume, and the brain sends signals for contraction of the detrusor muscle during micturition. Malfunction in these signalling events may underlie various bladder disorders such as Detrusor Overactivity and Overactive Bladder (OAB) (Birder et al., 2012). The mechanisms through which the urothelium senses and transduces information about physical stimuli are not well understood. However, it is clear that mechanical stress in urothelial cells plays a vital role; for instance, urothelial cells contain various receptors that respond to mechanical changes by the release of transmitters (such as ATP) that influence afferent nerve activity (Birder et al., 2009, 2012).

It is evident that the mechanical environment within the urothelium is critical to the proper functioning of the bladder, and that a balance must exist between vesicle trafficking, geometry, stress levels, and signalling. There is a delicate nature to this balance: exocytosis increases the surface area of the apical membrane, thus decreasing the tension, while at the same time, the appropriate amount of tension at the right bladder volume is

¹ NB in this article endocytosis refers specifically to pinocytosis.

needed to trigger afferent nerve activity and properly communicate the sense of “fullness” to the brain. To understand these relationships, how the system responds to abnormal stimuli, and where the root problem might lie in urinary tract disorders, mathematical modelling can have great value, both in providing qualitative insight and in guiding experimental directions. Yet despite a large amount of experimental and clinical research, there remains very little mathematical treatment of this complex mechanical system. While there have been several models concerned with different aspects of bladder mechanics (Damaser and Lehman, 1995; Korossis et al., 2009; Coldinq-Jørgensen and Steven, 1993; Damaser, 1999; Damaser and Lehman, 1996) or neurological signalling (Bastiaanssen et al., 1996; Fry et al., 2011; Bykova and Regierer, 2005), no models to date have been developed to consider exo-, endocytosis and the relationship between geometry, vesicle traffic, and cell level morphology.

In this paper, we develop a first model of the bladder umbrella cells to investigate the relationship between the mechanical environment in the urothelial tissue and vesicle trafficking within the umbrella cells. We derive a model specifically motivated by the experiments of Yu et al. (2009). In these experiments, a circular section of rabbit urothelium, with outer layers removed, was mounted in an Ussing chamber, and subjected to different mechanical forces. Tissue surface area was inferred from electrophysiological parameters, measured on time scales of less than a minute. This setup offers the distinct advantage of a closed in-vitro system in which umbrella cell activities are isolated and surface areas are quantified and monitored on short time scales. We focus on a particular experiment of that paper, in which a higher pressure head is applied in the mucosal hemichamber (the apical side), creating a fixed pressure difference across the uroepithelial tissue (see Fig. 2).

Our initial objective in this paper is to develop a mathematical model of vesicle trafficking and umbrella cell mechanics during bladder filling. We outline more thoroughly the relevant experimental detail of Yu et al. (2009), as well as our modelling approach, in Section 2. In Section 3, we first perform a quantitative comparison of the model predictions with experimental data and approximate unknown model parameters. We then provide a qualitative analysis of the vesicle dynamics, through which we gain insight into the physical nature of vesicle traffic and its relationship with membrane tension. The question then is how the vesicle dynamics function in a physiological setting, and whether certain pathologies might have as a root cause dysfunction at the level of vesicle traffic. To explore such issues, in Section 4 we translate the calibrated model to a spherical geometry to simulate in vivo bladder filling, and in this setting we demonstrate the

predictive potential of the model. Conclusions and extensions are discussed in Section 5.

2. Ussing chamber experiment and model description

2.1. Experimental description

In the experiments of Yu et al. (2009), a circular disc of rabbit uroepithelial tissue, with outer layers and smooth muscle removed so that only basal, intermediate and umbrella cells remain, is pinned between two sides of an Ussing chamber which is filled with a fluid (Krebs buffer solution). Each side connects to a vertical column of the same fluid, the height of which is kept constant by including an excess of fluid in a horizontal section of tubing (see Fig. 2(a)). By imposing a height differential of the tubing, the membrane is subjected to a fixed hydrostatic pressure difference; in particular, raising the height of the tubing into the mucosal hemichamber (i.e. the apical side) simulates filling of the bladder. We are particularly interested in the experiment described in Fig. 1E of Yu et al. (2009), in which the height of the tubing into the mucosal hemichamber is successively doubled from 1 cm to 16 cm. Note that in these experiments, the free end of the horizontal tubing is attached to a stopcock, which is removed at the start of the experiment, enabling for an ‘instantaneous’ pressure difference.

2.2. Experimental results

The experimental results given in Fig. 5A of Yu et al. (2009) are reproduced here in Fig. 2(b), where the percentage increase in capacitance across the apical membrane over the course of an hour is recorded. Capacitance is assumed to be in one to one correspondence with surface area, with $1 \mu\text{F}$ of capacitance approximately equal to 1 cm^2 of membrane surface area (Lewis and de Moura, 1982).

At all pressures, the membrane area changes in a non-monotonic manner. In the first minute the area increases rapidly, approximately doubling. This is followed by a decrease over the next several minutes to $\sim 125\%$ of the original surface area. The rates of both the area increase and subsequent decrease are higher with a larger imposed pressure difference. Following the decrease, the area then settles to a near equilibrium state, with a very small rate of change, such that over the course of an hour, there is a relatively small area increase, to around 130–150% of the original area.

The non-monotonic change in surface area is non-intuitive, and reflects a complex intracellular dynamic at play as the cells

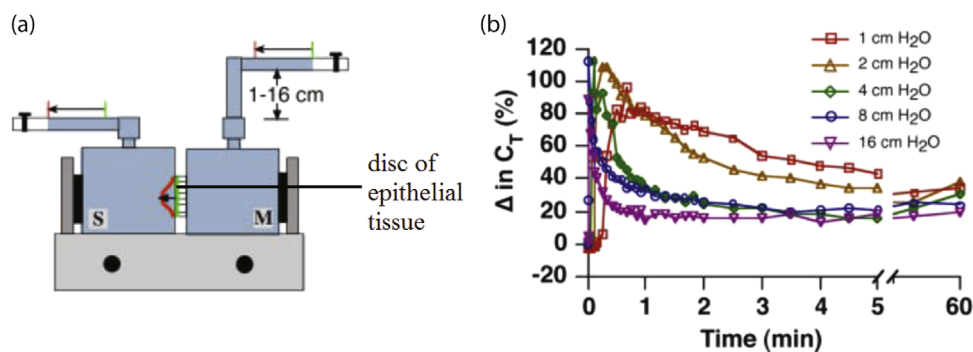


Fig. 2. (a) Experimental set-up: the height of the apical column is varied from 1 cm to 16 cm. The green line is the initial position of the excised uroepithelium and the red line the position upon bowing. M denotes the mucosal hemichamber (apical side) and S the serosal hemichamber (basal side). (b) Percentage change capacitance C_T measured against time at different pressures; as capacitance is assumed to be in one to one correspondence with surface area, this is a measure of evolving apical surface area. (For interpretation of the references to color in this figure, the reader is referred to the web version of this article.) Experimental setup (a) and results (b) adapted from Yu et al. (2009))

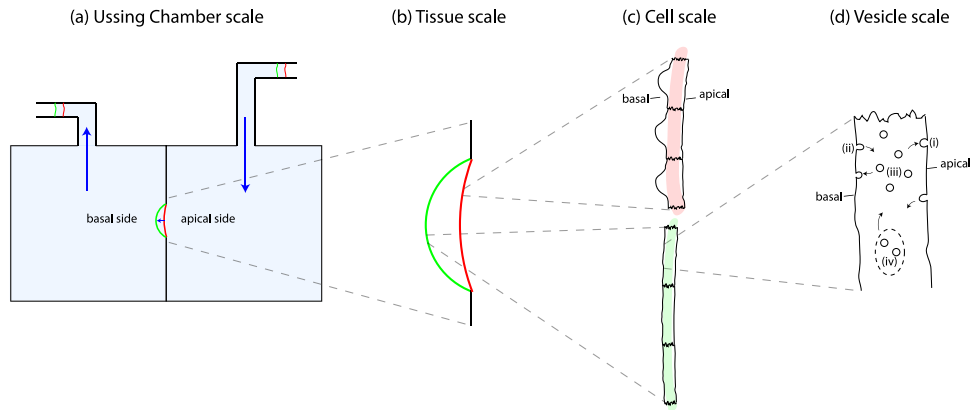


Fig. 3. Model schematic. An imposed pressure difference is applied in an Ussing chamber (a), causing the urothelial tissue, modelled as a spherical cap at the tissue level (b), to bow outward. The umbrella cells undergo a morphological change from goblet to squamous as the basal membrane unfolds (c); this is accompanied by insertion and removal of cytoplasmic vesicles in the cell membranes (d). Vesicles from the intracellular population (iii) may fuse with either the apical (i) or basal (ii) populations; after endocytosis vesicles are sent to a “recycling” population (iv) before returning to the intracellular population.

respond to the instantaneous pressure difference. Surface area will change as a result of both vesicle trafficking, i.e. an increase or decrease in the amount of membrane material, and mechanical stretching of the tissue; measuring area (or capacitance) alone is not enough to distinguish between the two effects. The explanation suggested by the authors for the non-monotonic behaviour is that both exo- and endocytosis occur in the apical membrane, with tension in the apical membrane causing exocytosis and tension in the basal membrane causing endocytosis. A key feature in this process is the change in shape of the umbrella cells. Initially, the basal side is curved, hence only the apical side is supporting tension. As the tissue bows outward (or as the bladder fills), the cell changes to a squamous shape (see Fig. 3(c) and also compare the yellow dashed line in Fig. 1). Mechanically, we can interpret this in the sense that the basal membrane must ‘unfold’, i.e. there is a critical displacement required before the basal membrane begins to support any tension.²

Varying the pressure does not significantly affect the magnitude of the maximum bowing, an experimental observation that has been used to suggest that the maximal bowing is purely a property of the length of the basal membrane, i.e. that the basal side of the umbrella cells do not experience any vesicle trafficking and that the maximal bowing corresponds to the point of unfolding (Yu et al., 2009).

2.3. Model description

Our objective is to build a mathematical model that can discriminate between the hypotheses stated above and yield insight into the relationship between the mechanical environment of the umbrella cells and vesicle trafficking.

A schematic of our modelling approach is given in Fig. 3. A full derivation is given in Appendix A; here we provide an outline. At the scale of the Ussing chamber, Fig. 3(a), we use a Poiseuille flow description in the two cylindrical tubes to determine the flow rates in and out of each chamber. The section of horizontal tube ensures a fixed hydrostatic pressure at the top of each column of water, and we assume that the pressures felt by the membranes on either side of the chamber are equal to the pressure at the bottom of the tube.

At the tissue scale, Fig. 3(b), we model the uroepithelial tissue

as a spherical cap. The surface area, radius of curvature, and volume contained within the bowed cap can all be written in terms of a single geometric variable, the maximum tissue deflection on the apical side, denoted $h_a = h_a(t)$. The rate of change of cap volume is equated to the flow rate from the Poiseuille description. In this way, the deformation rate satisfies

$$\frac{d}{dt}h_a(t) \propto (\Delta P - \Delta p), \quad (1)$$

where ΔP is the fixed and imposed pressure difference, while Δp is the pressure difference across the urothelial tissue.³ The general idea of the model is as follows: we relate the pressure difference Δp to the tension in each membrane; the membrane tension drives vesicle traffic; the vesicle traffic serves to change the reference areas of the membranes; the varying reference area affects the degree of stretch, which then feeds back to change the tension and pressure.

On the cellular scale, Fig. 3(c), we consider the apical and basal sides of the umbrella cell as two distinct tension supporting membranes. We assume that at time $t=0$ the apical membrane is in an unfolded (flat) zero tension state, while the basal membrane is curved and does not support any tension until a geometric unfolding point is reached (see Appendix A). Starting from energy considerations, we show in Appendix A that membrane stretching is dominant to bending in this setup, and thus that the pressure difference across each membrane is approximately balanced by the membrane tension via a Young-Laplace-like relation. Applying this relation across both the apical and basal membranes, assuming a constant intracellular pressure, yields

$$\Delta p = \frac{2T_a}{r_a} + \frac{2T_b}{r_b},$$

where $r_{a,b}$ are the radii of curvature of the apical and basal membranes, and $T_{a,b}$ the respective tensions. The geometry enables the radii of curvature to be written in terms of h_a . The tension in each membrane is a linear function of the areal stretch: the area of the membrane divided by its reference (unstretched) area. The former can be written as a function of h_a , while the latter depends on vesicle traffic, i.e. the amount of membrane material that has been added or removed from the membrane. This requires a

² There is also an unfolding process of much smaller folds on the apical membrane, though these folds are less apparent in the mounted Ussing chamber tissue compared to in vivo and will thus not be included in our modelling development.

³ We remark that the intermediate and basal cell layers are also present in the experiments. However, any membrane trafficking events that may occur in these cell layers do not contribute to the surface area changes described for the umbrella cell layer, and their role in area modulation is unclear. For simplicity they are excluded from our model, an assumption further discussed in Section 5.

description of the insertion (exocytosis) and/or removal (endocytosis) of cytoplasmic vesicles.

Hence, the final component of our model is a description of vesicle traffic within the umbrella cells. Within the cell cytoplasm, there is an abundant pool of vesicles, comprised of both newly synthesized vesicles that may be delivered to either the apical or basal surface, and vesicles that are formed upon apical or basolateral membrane endocytosis, and which may undergo another round of exocytosis or may be delivered to lysosomes for degradation (Apodaca, 2003). For simplicity, we consider four distinct populations of vesicles, shown schematically in Fig. 3(d): vesicles that have fused with the apical (i) or basal (ii) membrane, intracellular vesicles that are available for exocytosis (iii), and endocytosed vesicles that are being “recycled” before further rounds of exocytosis (iv).

We assume that the total surface area of all vesicles combined remains at a fixed value (Truschel et al., 2002), and track the proportion of vesicles in each of the different states. Note that these four states are not meant to represent a complete description of all possible vesicle activities and pathways, for instance we do not explicitly account for transcytotic traffic (i.e., transport of endocytosed membrane between surface domains), vesicle degradation/synthesis, or distinct apical and basal vesicles. Such a description would introduce an excess of unknown parameters. Rather, our approach is to form a lumped description of vesicle traffic with minimal parameters that can capture the observed behaviour and enable an understanding of the feedback between the mechanical environment of the deforming cells and vesicle traffic. To this end, we propose a simple model for exo- and endocytosis in which the rate of change of the proportion of vesicles in any given state is a function of the tension within the membrane walls. This general idea is well-supported across many cell types (Morris and Homann, 2001), and in particular is motivated by experimental evidence that apical tension stimulates apical exocytosis and basolateral tension stimulates apical endocytosis (Yu et al., 2009) in umbrella cells. Here we extend this by hypothesising that basal tension could also stimulate basal exocytosis and that apical tension could stimulate basolateral endocytosis. While this idea is less intuitive, its feasibility may be inferred from experimental evidence (Yu et al., 2009; Khandelwal et al., 2008), and from reports that mechanical forces are communicated between the surfaces of epithelial cells (Ingber, 2003; Wang et al., 2001). A key modelling objective will be to determine whether this model component is necessary to reproduce observed behaviour.

The description above is expressed by the system

$$\begin{aligned} \frac{d}{dt}\phi_a &= \frac{k_{aa}}{\mu_a}\phi_c T_a - \frac{k_{ab}}{\mu_b}\phi_a T_b, \\ \frac{d}{dt}\phi_b &= \frac{k_{bb}}{\mu_b}\phi_c T_b - \frac{k_{ba}}{\mu_a}\phi_b T_a, \\ \frac{d}{dt}\phi_c &= k_R\phi_R - \phi_c \left(\frac{k_{aa}}{\mu_a}T_a + \frac{k_{bb}}{\mu_b}T_b \right), \\ \frac{d}{dt}\phi_R &= \frac{k_{ab}}{\mu_b}\phi_a T_b + \frac{k_{ba}}{\mu_b}\phi_b T_a - k_R\phi_R. \end{aligned} \quad (2)$$

Here $\phi_{a,b,c,R}$ represent the proportion of the total vesicle population in states (i)–(iv), respectively. The constants $k_{\alpha\beta}$ characterise the rates of the different trafficking events, in particular the rate of vesicle traffic on the α side due to tension on the β side, with $\alpha = a, b; \beta = a, b$. The $\mu_{a,b}$ are the membrane stiffnesses; these constants are included so that the parameters $k_{\alpha\beta}$ have units consistent with actual rates. The constant k_R denotes the rate at which endocytosed vesicle membrane is returned to the intracellular population for additional rounds of exocytosis. The

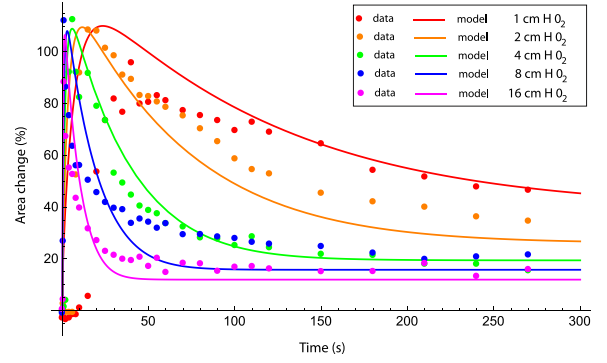


Fig. 4. Area change data vs output of model for varying pressures. Data reproduced from Yu et al. (2009) appear as closed circles, the solid lines represent the model output at corresponding values of the imposed pressure difference across the Ussing chamber. Each model output is produced using the single set of best fit parameters, as described in Appendix E. (For interpretation of the references to color in this figure, the reader is referred to the web version of this article.)

multiplying factors ϕ_α reflect the notion that vesicle traffic occurs in rates in proportion to the amount of vesicle material available in each of the different states, and ensures that each $\phi_\alpha \in [0, 1]$. Thus, the first equation, for example, states that the apical vesicle pool will increase (apical exocytosis) due to apical tension, but only if intracellular vesicles are available ($\phi_c > 0$), and will decrease (apical endocytosis) due to basal tension, but only if apical vesicle membrane is available to be endocytosed ($\phi_a > 0$).

The system is such that $\frac{d}{dt}(\phi_a + \phi_b + \phi_c + \phi_R) = 0$, and hence without loss of generality $\phi_R = 1 - (\phi_a + \phi_b + \phi_c)$ can be eliminated. Letting \mathcal{A} denote the total vesicle area i.e. the area of all vesicles combined, the unstressed area of the apical membrane satisfies

$$A_a(t) = A_a(0) + \phi_a \mathcal{A},$$

where $A_a(0)$ is the initial apical area, and the stretch is then the ratio of the geometric area to this quantity. A similar relation holds for the basal membrane. In this way, given a constitutive law relating the tensions $T_{a,b}$ to membrane stretch, we can express the tensions as functions of $h_a(t)$, $\phi_a(t)$, and $\phi_b(t)$.⁴ We thus have a closed system of 4 coupled ordinary differential equations for $h_a(t)$, $\phi_a(t)$, $\phi_b(t)$, $\phi_c(t)$. In solving the system, we assume that all vesicles initially begin within the intracellular population, and h_a is given a small but non-zero initial value (non-zero to avoid an infinite radius of curvature at $t=0$).

3. Model behaviour

In this section we consider the general behaviour of the model and identify those processes that are needed to reproduce the experimental observations. As a starting point, we first perform a quantitative comparison with the varying pressures experiment of Fig. 5A in Yu et al. (2009) to determine a base set of parameters. We then analyse the qualitative behaviour of the model and the balance between geometry, mechanics, and vesicle traffic.

3.1. Parameters and data fit

We begin by using a quantitative comparison with experiment to calibrate the model. Most parameters are provided in the

⁴ Note that as stated above, the basal tension only exists after the basal side has unfolded, hence the constitutive form for the basal tension includes a geometric switch such that $T_b=0$ until a critical displacement, h_a^* , is reached.

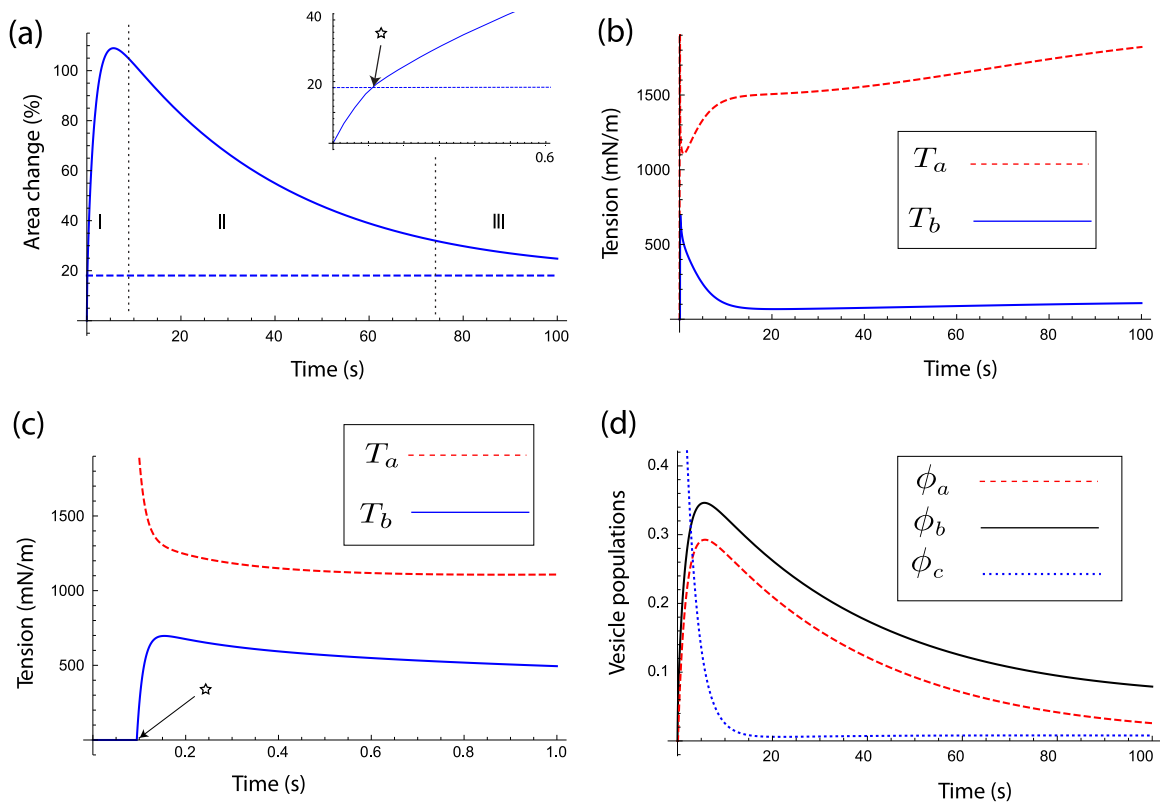


Fig. 5. Qualitative behaviour of the model. (a) Percentage area change, with the different phases separated by dashed vertical lines. The horizontal dashed line represents the area at which the basal membrane is unfolded. The inset gives a close-up at early times. Apical and basal tensions are plotted on the time scale of 100 s (b) and 1.0 s (c), with the point of basal unfolding marked by a star. (d) The vesicle populations ϕ_a , ϕ_b , ϕ_c (the recycling population ϕ_R satisfies $\phi_R = 1 - \phi_a - \phi_b - \phi_c$). Parameters are as in Table D2 in Appendix D.

experiment or can be well approximated from the literature. The parameters about which we have the least knowledge are the vesicle trafficking rate parameters, which were determined by fitting the model output to the experimental data (see Appendix E for details on fitting). The model output of area change against time is overlaid on the data in Fig. 4. The best fit parameter values form the base set for the remainder of this paper. A full list of parameter values is provided in Appendix D. To assess the sensitivity of the model to the base values, we have also performed a detailed sensitivity analysis (Appendix F), from which we find that the output is reasonably robust with respect to variation from the base parameters. To better understand intuitively the impact of the different parameters and model components, we now assess the qualitative behaviour of the model.

3.2. Qualitative behaviour

The dynamics consist of three distinct phases, marked in Fig. 5 (a) and discussed in detail below. In capturing each phase, we identify necessary components of the model and features of the vesicle trafficking process that underlie the observed behaviours.

3.2.1. Phase I – Exocytosis

The initial response to the imposed pressure difference is net exocytosis and a rapid bowing of the tissue on a timescale of seconds. In the early part of this stage (within the first second or two), only the apical side is active, while the basal side is ‘unfolding’ due to the changing cell morphology. The apical tension is correspondingly very high, but is tempered by apical exocytosis (ϕ_a increases). Once the basal side unfolds, the basal membrane supports some of the pressure, thus the basal tension rises sharply and the apical tension drops, as seen in Fig. 5(b). With the basal

side unfolded, there are two membranes supporting tension, and the bowing rate is somewhat decreased (see inset in Fig. 5(a)), though it continues to rise sharply. At this point, both membranes are rapidly recruiting intracellular vesicles, hence ϕ_a and ϕ_b both increase while the intracellular population ϕ_c decreases sharply (Fig. 5(d)).

As seen in Eqn. (1), the bowing phase is marked by $\Delta P > \Delta p$, and the criterion for bowing to stop is that the membrane pressure difference Δp must ‘catch up’ with the imposed pressure difference ΔP . While the tissue is bowing, the radii of curvature are decreasing.⁵ If there were no exocytosis, the membranes could only accommodate bowing by stretching. The tensions and hence Δp would increase rapidly, and the tissue would stop bowing after only a small increase in area. In fact, a simple calculation (Appendix G) shows that with no exocytosis, the tissue would only increase its area by approximately 3%! Exocytosis enables bowing to occur with only moderate tensions. This illustrates clearly the role of exocytosis in allowing the tissue to accommodate a much larger deformation.

The maximum bowing is coupled to the rates of exocytosis. In Fig. 6(a), we plot the apical area change – defined as $(A_a(t) - A_a(0))/A_a(0)$ – using base values for k_{aa} and k_{bb} and with each rate doubled. Increased exocytosis rates lead to approximately an extra 20% in the maximum area. We also show in Fig. 6 (a) the effect of doubling the total vesicle pool: the maximum area also doubles. This suggests that the maximum bowing is more strongly driven by the total area of all vesicles. Rather than keeping the ‘extra vesicles’ stored within the intracellular

⁵ This is particular to the spherical cap geometry. The tissue begins as a flat disc, with ‘infinite’ radius of curvature, and the radius of curvature continues to decrease until a hemispherical state is reached.

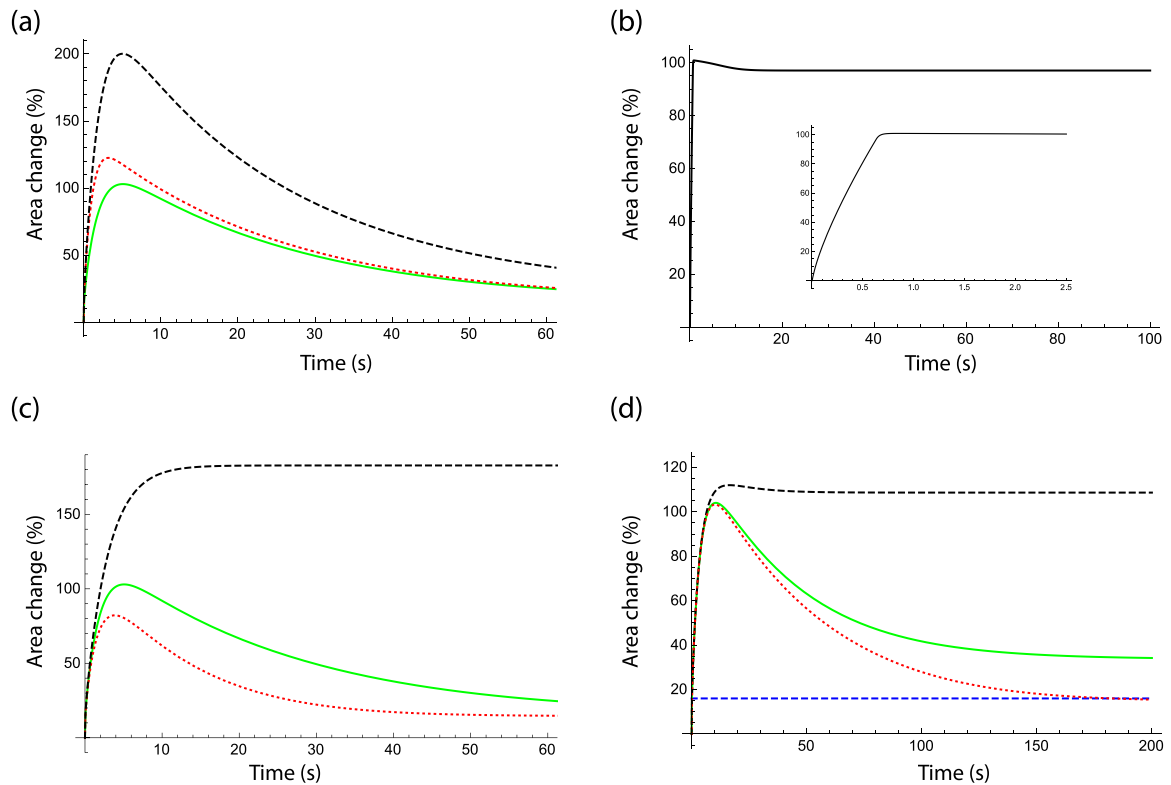


Fig. 6. Qualitative effect of model parameters on percentage area change, compared to the base case (solid green curves). (a) Effect of doubled exocytosis rates k_{aa} and k_{bb} (red dotted) and doubled vesicle pool \mathcal{A} (black dashed); (b) an increased unfolding point and zero basal traffic gives a nearly monotonic behaviour; (c) the effect of varying endocytosis rates k_{ab} and k_{ba} : doubled (red dotted) rates and zero endocytosis (black dashed); (d) the effect of vesicle recycling rate k_r : a 10 fold increase (black dashed) and 100 fold decrease (red dotted). The dashed horizontal line marks the area change at the basal unfolding point. Base parameters are as in Table D2 in Appendix D. Applied pressure parameter $L_a=4$ cm in (a)– (c), $L_a=2$ cm in (d) (smaller value used to amplify recycling rate effect). (For interpretation of the references to color in this figure, the reader is referred to the web version of this article.)

population, with more vesicles available, more vesicles are used.

We can also see the necessity of basal exocytosis in reproducing the experimental behaviour. Observe that the maximum area increase is around 100% for the base parameter set, after which the area drops back to around a 30% increase. From cell geometry considerations (Appendix C), we compute that the basal side begins supporting tension when the area has increased by approximately 20%. In order to increase by 100%, if there were no basal traffic, the extra 80% would have to be accommodated by stretching of the basal membrane. A simple calculation gives that this would require a stretch of around 60%, which is far past the threshold for tearing.

However, it might be that we have underestimated the unfolding point. This would be in line with the suggestion in Yu et al. (2009) that the maximum area, which is roughly independent of the imposed pressure, is determined purely by geometry and corresponds with the unfolding point of the basal membrane. In that case, however, while there would be no issue with the tissue bowing to an area increase of 100%, the subsequent drop to 30% area increase would not occur, because as soon as any decrease in area occurred, the basal side would cross back below the unfolding threshold, basal tension would vanish, and hence apical endocytosis would cease. A sample simulation with basal exo-, endocytosis turned off ($k_{bb} = k_{ba} = 0$)⁶ is given in Fig. 6(b), showing a nearly monotonic behaviour.

3.2.2. Phase II – Endocytosis

Once $\Delta p = \Delta P$, the tissue stops bowing ($dh_a/dt = 0$). However,

⁶ Actually, it is sufficient to set $k_{bb} = 0$. Without exocytosis, the basal membrane never adds any vesicles and thus has zero endocytosis as well.

as seen in Fig. 2(b), it does not reach this point asymptotically, but rather as a turning point, with the tissue switching from an increase to a decrease in area, on a timescale of minutes. From a physiological standpoint, such non-monotonic behaviour seems non-intuitive. Why does the tissue not attain an equilibrium when the pressures are in balance?

First, it is worth noting that at the turning point, $d\phi_a/dt \approx d\phi_b/dt \approx 0$ (see Fig. 5(d)), thus the apical and basal membranes are approximately in equilibrium as well, meaning the rates of exo- and endocytosis are in balance. However, as the tensions are non-zero, each side continues to recruit vesicles and so $d\phi_c/dt < 0$. Hence the system is not in equilibrium. Rather, the scales become tipped in favour of endocytosis and the area starts to decrease. Note that this would not be the case if endocytosed vesicles were immediately available for re-use. That is, if there were no ‘recycling’ population, the geometric balance, combined with zero net traffic in the apical and basal membranes, would imply an intracellular balance as well ($d\phi_c/dt = 0$), and the system would be in equilibrium. Concurrent with this, simulations with state (iv) removed are marked by a monotonic increase in area.

Secondly, that the endocytosis phase is observed experimentally is strongly suggestive of mechanical coupling between the apical and basal membranes. That is, we find the important result that non-monotonic behaviour is not possible if basal tension only affects basal traffic and apical tension only affects apical traffic, i.e. if the cross terms in Eq. (2) vanish ($k_{ab} = k_{ba} = 0$). These terms link apical endocytosis to the basal membrane, and vice versa. Moreover, the rate of area decrease is primarily determined by these values, such that an increase in these values causes a sharper drop in area (see Fig. 6(c)).

3.2.3. Phase III – levelling and equilibrium

As well as having $d\phi_c/dt < 0$, the decrease in tissue area during Phase II is characterised by a decrease in basal tension and increase in apical tension. As seen in Fig. 5(b), during Phase II tension rises on the apical side, as the net loss of membrane material due to endocytosis outpaces the decrease in area. By contrast, on the basal side, the area decrease dominates and the tension decreases. Eventually, the intracellular population stops decreasing and plateaus (see Fig. 5(d)), meaning that the number of vesicles being returned from recycling approximately matches the number being exocytosed. Beyond this point, all quantities evolve monotonically, and the system settles to an equilibrium over a timescale of tens of minutes. This equilibrium state represents a simultaneous balance of the imposed pressure with the membrane pressure difference, and the gain and loss of vesicles in each population. In terms of rate parameters, the tissue area at equilibrium is most strongly influenced by the recycling rate k_R , which provides a time delay for the return of vesicles to the pool. An example is given in Fig. 6(d), where area change is plotted for increased and decreased values of k_R . As $k_R \rightarrow 0$, the rate of return of vesicles to the intracellular population vanishes; hence there is no replenishing of vesicles, the second turning point does not occur, and the equilibrium state is close to the unfolding point. On the other hand, with immediate recycling (equivalent to $k_R \rightarrow \infty$), the behaviour is monotonic; accordingly, for large k_R the area decrease is small and the equilibrium balance occurs at a large area increase.

Finally, recall that the experiments also display a final phase, involving a very slow and mild increase in surface area over a time scale on the order of an hour. As this is likely connected to the synthesis of new vesicles (Truschel et al., 2002), which we do not explicitly include, this final phase is not predicted by the model. Although new vesicle production could easily be incorporated into our framework, it would have little effect on the early time dynamics and would require the introduction of an additional parameter, hence we have chosen to neglect this phase.

4. Physiological simulations

Having established a qualitative understanding of the interactions between geometry and mechanics in vesicle trafficking, and reasonable estimates for the rates of exo- and endocytosis, we now show how the model can be adapted to simulate a more physiological bladder filling process.

4.1. Spherical model

To simulate filling, we model the bladder as a full sphere. While this is an idealisation, a spherical geometry has been utilised in previous models (Damaser, 1999) and has been shown to be a reasonable approximation (Damaser and Lehman, 1995) in fitting pressure-volume changes during late stage, quasistatic filling. The basic structure of the model is the same, with details provided in Appendix A.1. There are, however, two key conceptual differences in moving from bladder tissue in an Ussing chamber to an in vivo scenario. Firstly, there is a critical geometric difference in the nature of the spherical symmetry: bowing of the spherical cap in the Ussing chamber causes a decrease in the radius of curvature, while bowing of the full bladder sphere during filling increases the radius of curvature. This difference can be appreciated by considering bowing due to a constant pressure and in the absence of exocytosis. If a sphere expands due to a constant applied internal pressure, the tension increases, since it is proportional to pressure times radius of curvature and the radius of curvature increases. By contrast, an expanding spherical cap will experience a decrease in

tension due to the decreasing radius of curvature.⁷ Hence the relationship between curvature and tension, following the Young-Laplace relation, is inverted. To see the impact of these differences, we simulate a sphere expanding due to an imposed pressure and an expanding cap under an equivalent pressure. While a direct comparison is difficult due to the differing geometries, we fix the initial radius of the sphere equal to the disc radius, keep all rate parameters the same, and set the basal unfolding point in the sphere such that it occurs at the same relative area increase as in the cap model. The results are presented in Fig. 7, where we plot the apical tension at early and long times, as well as the percent area change. We note that while the tension curves are dissimilar, and have opposing gradients over much of the dynamics (Fig. 7 (a)–(b)), the geometric behaviour is almost identical (Fig. 7(c)–(d)).

A fixed imposed pressure was used in Fig. 7 to enable a direct comparison between the cap and sphere models. However, this highlights the second key difference: while the Ussing chamber experiments may be thought of as pressure driven, due to the fixed column of fluid, this is not the case for a filling bladder. The bladder fills due to urine being delivered from the kidneys via the ureters, tubes of smooth muscle fibres that propel the urine along. This is quite different from a column of fluid entering a chamber due to gravitational forces. Rather, the filling of the bladder is better understood as a volume driven process. Hence, in simulating physiological bladder filling, it is more appropriate to take as input a given ‘filling curve’, i.e. the bladder volume as a function of time. This change simplifies the model in that the geometry is no longer determined as the solution of a differential equation, as in the Ussing chamber description, but rather follows a prescribed functional form. For simplicity, in all simulations below we assume a linear increase in volume with time, such that the bladder increases from 113 mL to 339 mL.⁸

4.2. Bladder filling and innervation

Critical to proper functioning of the bladder is communicating the sense of ‘fullness’ to the nervous system. The signalling mechanisms by which information about the mechanical environment within the bladder are communicated to the brain are complex and poorly understood (Birder et al., 2009). Of particular relevance is the presence of receptors and afferent nerve fibres in the urothelium, whose activity is strongly driven by mechanical changes and likely connected to ATP release (Apodaca, 2003; Birder et al., 2012).

Our objective is not to explicitly model the mechanotransductive pathways and signalling events. Rather, we take a phenomenological approach: by monitoring membrane tension and positing a causal relationship between tension and signalling, we aim to investigate the effect of changes in the vesicle trafficking machinery on the signalling mechanism. For simplicity, in what follows we assume that innervation occurs when the tension increases past a threshold value – here we use a threshold value of 1 mN/m, which is a typical tension at which activation of mechanosensitive channels occurs in non-specialised cells (Sachs and Morris, 2015; Morris and Homann, 2001). The basic simulation is as follows: we prescribe a volumetric filling rate, solve the governing equations, and plot the tension.⁹ By noting when the signalling threshold is crossed for different parameter regimes, we can infer consequences of changes in the vesicle machinery on the

⁷ Note this statement only holds for a cap deforming from a disc up to the point of a hemisphere, beyond which point the radius of curvature increases. However, the experiments suggest that the tissue does not deform beyond the hemispherical point.

⁸ Equivalent to an initial radius of 3 cm and a tripling in volume.

⁹ Here we restrict to the apical tension; the basal tension follows a similar form.

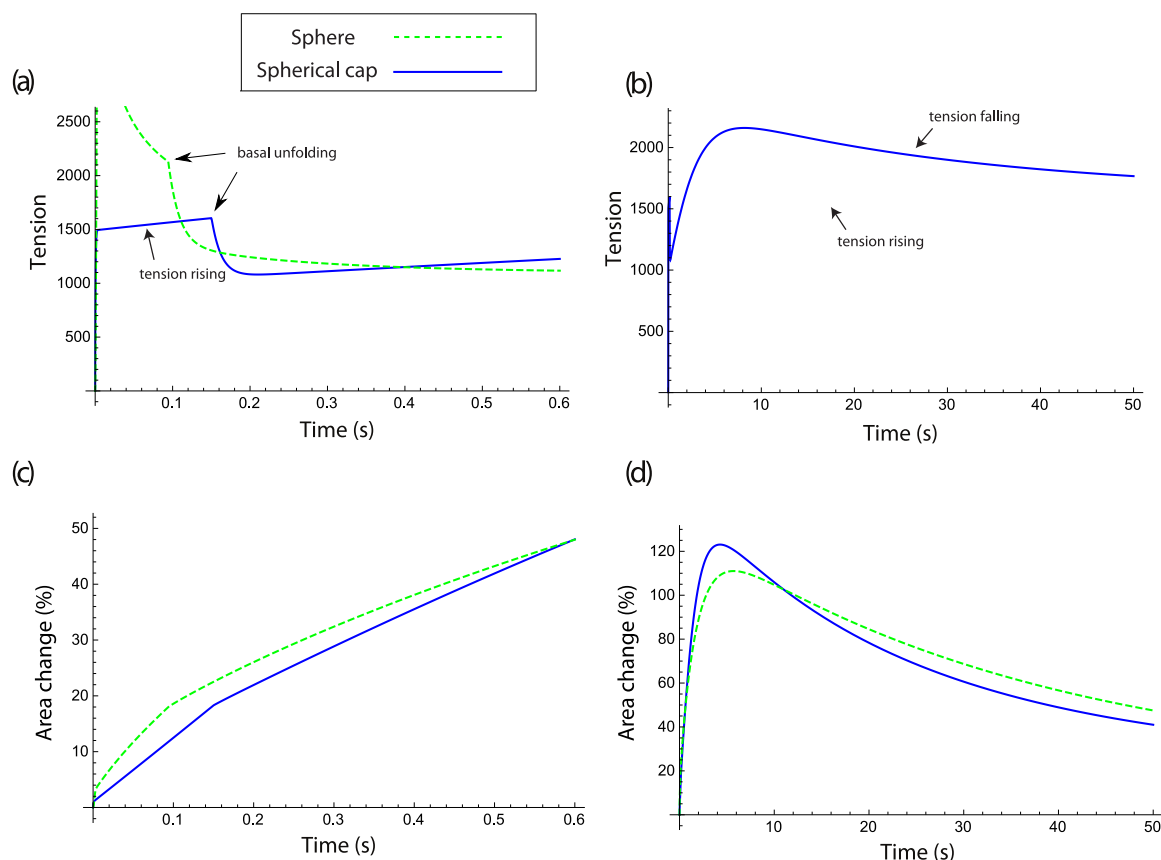


Fig. 7. Comparison of pressure-driven full sphere filling (green dashed) versus pressure-driven bowing of spherical cap (blue solid). Apical tensions at early (a) and later (b) times, and apical area change as percentage at early (c) and later (d) times. Parameters are as in Tables in Appendix D. (For interpretation of the references to color in this figure, the reader is referred to the web version of this article.)

communication of fullness.

4.2.1. Filling rate

We first consider the effect of the volumetric filling rate. We consider three different filling rates, shown in Fig. 8(a), and the time evolution of the corresponding tensions in Fig. 8(b). The dashed horizontal line is the tension threshold at which we posit a signalling event would occur. For discussion purposes, we treat the green solid curve as the base case, and suppose this corresponds to a 'healthy' bladder. Here, the volume increase takes place over the course of two hours, and the signalling threshold is crossed when the bladder is 93% full. With an increased filling rate – the same

total volume change over only an hour – the maximum stress is much higher, and the signalling threshold is crossed much earlier, when the bladder is only 70% full. Hence a stronger sense of urge would be felt and for a longer period of time, even with the bladder far from being full. If the filling rate is decreased, on the other hand, the peak tension never crosses the threshold and the signal of a full bladder is never sent, even though the bladder reaches the same total volume.

4.2.2. Exocytosis rate

The rate of exo-, endocytosis directly impacts the vesicle dynamics, and thus can have a strong effect on the tension levels

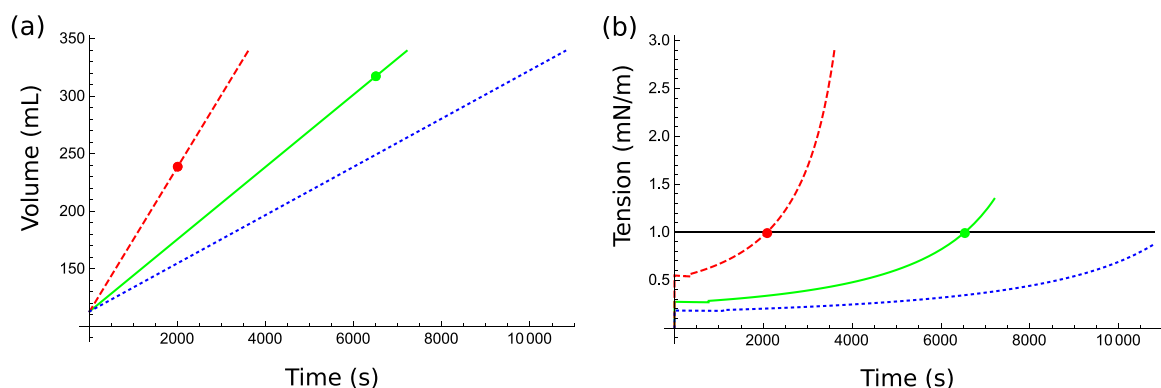


Fig. 8. The effect of volumetric filling rate on tension. (a) Linear filling with three different rates: 0.02, 0.03, 0.06 mL/s for blue-dotted, green, red-dashed, respectively, and (b) corresponding tensions plotted against time. The horizontal line represents a signalling threshold, and the dots indicate the point at which the threshold is crossed in each case. (The apparent discontinuity in the curves toward the left side corresponds to the basal unfolding point, and only appears discontinuous at the scale presented.) Parameters are as in Tables in Appendix D. (For interpretation of the references to color in this figure, the reader is referred to the web version of this article.)

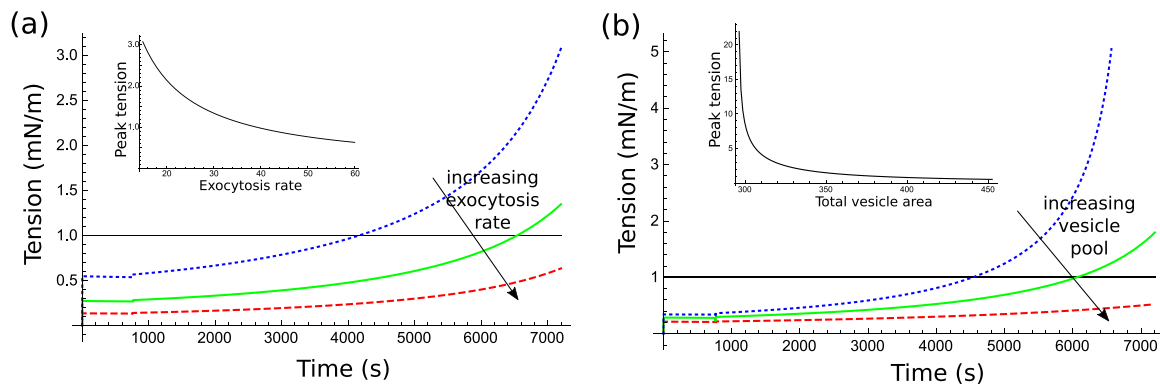


Fig. 9. Effect of apical exocytosis rate and total vesicle area on tension during simulated spherical bladder filling. (a) Varying exocytosis rates: $k_{aa} = 15, 30, 60$ for blue-dotted, green, red-dashed, respectively. Inset: peak tension as a function of k_{aa} . (b) Varying total vesicle area: $A = 318, 356, 452$ cm^2 for blue-dotted, green, red-dashed, respectively. Inset: peak tension as a function of total vesicle area. (The apparent discontinuity in the curves toward the left side corresponds to the basal unfolding point, and only appears discontinuous at the scale presented.) Volumetric fill rate 0.03 mL/s in all cases, other parameters are as in Tables in Appendix D. (For interpretation of the references to color in this figure, the reader is referred to the web version of this article.)

during filling. An example is shown in Fig. 9(a), where we plot the time evolution of apical tension for three different apical exocytosis rates, each with the same volumetric filling rate, corresponding to the base solid green curve in Fig. 8. The baseline rate was doubled and halved, with all other parameters held fixed. As might be expected, a higher exocytosis rate leads to lower tension, and vice versa for a lower rate. The relationship between exocytosis rate and peak tension is shown as the inset in Fig. 9(a): this seems to indicate a saturation in decreasing tension with respect to increased exocytosis.

4.2.3. Vesicle population

Equally important in the uroepithelium's response to the filling bladder is having the necessary vesicle resources. If there are not enough intracellular vesicles present, the rising volume cannot be properly accommodated. In Fig. 9(b), we plot the tension during a filling cycle for three different total vesicle areas, each following the volumetric filling rate corresponding to the base solid green curve in Fig. 8. Here again we find that either too few or too many vesicles could be detrimental. With an excess of vesicles, the system is too quick in responding to the volume change and the tension never crosses the threshold, thus a signal is never sent. With a shortage of vesicles, the system cannot keep up with the vesicle demand, and the tension rises to several times the baseline value.

5. Discussion

In this paper we have developed a mathematical model for vesicle trafficking in the umbrella cells that comprise the outermost layer in the bladder uroepithelium. Our primary objective has been to elucidate the relationship between mechanics, geometry, and exo- and endocytosis of intracellular vesicles during bladder filling. More generally, this analysis attempts to develop a biophysical understanding of how mechanical forces influence cell level activity.

The motivation for our model development was the Ussing chamber experiments of ref. Yu et al. (2009). These experiments, conducted on a disc of rabbit uroepithelium tissue, showed the intriguing and non-intuitive behaviour of a non-monotonic area change in response to an imposed pressure difference across the two chambers of the Ussing apparatus. We first used the in vitro experiments to establish a minimal set of biophysical mechanisms and to estimate vesicle trafficking rate parameters via a quantitative fit with the data. In analysing the qualitative behaviour, we

uncovered several features that the model predicts need be present in the vesicle trafficking mechanism. First, we have verified the coupling between tension in one membrane and vesicle traffic in the other membrane that was hypothesised in part by Yu et al. (2009). Further, we found that significant basal exo- and endocytosis is required, a feature that had not been previously reported. We have also demonstrated the necessity of vesicle recycling in capturing the non-monotonic behaviour – as opposed to either immediate re-use of vesicles or vanishing vesicles upon endocytosis. Such findings may be of interest from the general viewpoint of understanding vesicle trafficking in epithelial cells, though in this regard a valuable next step would be to model more explicitly distinct vesicle populations, transcytosis events, and to include vesicle degradation and synthesis.

Having calibrated our biophysical description with the Ussing chamber experiments, we then adapted the model to physiological in vivo bladder filling to study the impact of imbalances and disruptions in the processes involved. We have noted two important physical differences between a full bladder and a disc of bladder tissue in an Ussing chamber. An expanding sphere increases its radius of curvature, while a disc expanding to a hemisphere decreases the radius of curvature. This change creates an inverted trend in the relationship between curvature and tension following the Young-Laplace law for the membrane, and thus can change significantly the dynamic tension levels during an area change. Nevertheless, it is noteworthy that in simulating a full sphere version of the Ussing chamber, this difference had little effect on the geometrical behaviour. Thus, in observing just the geometry, one could be misled to believe that the systems were behaving equivalently.

The other difference we noted was that while the Ussing chamber experiments we have analysed are driven by a fixed pressure difference across the chambers, the physiological filling of a bladder is more appropriately described as a volume driven process. Thus, in Section 4 we adapted the model to simulate a filling spherical bladder driven by an imposed linear volumetric filling rate, and considered the effect of variations in the vesicle trafficking machinery. In particular, we focussed on changes in the volumetric filling rate, the rate of apical exocytosis, and the total pool of available vesicles. The question of interest is how these changes might show their effect at the system level, in particular on the process of communicating the sense of 'fullness' to the brain. To do this, we posited a threshold tension at which signalling is triggered. Then, by tracking the tension during filling we can infer the likelihood of signalling events. While we have only considered the link between tension and innervation, of equal

importance is the bladder's barrier function; here it is to be noted that the tension is in a one-to-one relationship with stretch, thus a large tension is not only indicative of excessive signalling but also will be linked to a decreased barrier function.

In the simulations presented in Figs. 9, similar qualitative behaviour was observed with each parameter change: if the exocytosis rate or vesicle populations are at abnormal levels, the membrane tension can be significantly impacted, with important consequences for the functionality of the bladder. In each case, we find that signalling may occur well before the bladder is full. These symptoms are typical of those associated with Overactive Bladder (OAB), which suggests the hypothesis that dysfunction at the level of vesicle traffic might be at the core of OAB.

While the level of modelling presented in this paper is certainly idealistic, it has strong potential to be of clinical value. For instance, the sensation of urge is the key feature of OAB, but remains a phenomenon that is difficult to even define (Brubaker, 2004). It is suspected that urge is connected to afferent nerve activity, and might be understood in terms of malfunctioning vesicle dynamics. If this is the case, natural questions are how would one determine where *exactly* the problem lies and how should one address it. To this end, we consider two hypothetical patients with OAB, one due to diminished exocytosis rates and the other with a depleted vesicle pool. Can our model distinguish between the pathologies? Following the clinical methods in Oliver et al. (2002), we could ask the patients to record urge scores while measuring volumetric fill rates during filling cystometry. Each patient records urge scores during slower bladder filling, and again during rapid filling. The model simulations for these scenarios are shown in Fig. 10. We have chosen the parameters (i.e. degree of abnormality) such that the peak tension levels match in the slower filling. With the slow fill, the patient with the diminished exocytosis rate feels an initial urge about 30 min earlier than the patient with the depleted pool. As would be expected, the tension rises to higher values with the rapid filling rate, so that both patients would record higher urge scores in that round. Here, the patient with the depleted pool experiences a higher peak tension. However, it is the early time tensions at which we find a key difference: the patient with diminished exocytosis crosses the urge threshold almost immediately, within the first minute, while the patient with a depleted vesicle pool does not cross the threshold for close to half an hour. Mechanically, this relates the fact that the diminished exocytosis cannot keep up with the increased filling and thus the tension is high from the onset, while with the depleted vesicle pool the early filling can be accommodated and the detrimental effect is not felt until later times when the vesicle reserves get low.

In this simple example, we conclude that the different parameter regimes do indeed have different signatures, that could in theory be distinguished with standard clinical techniques.

Limitations and extensions. The above example demonstrates the potential of mechanistic modelling, while the examples considered in Section 4 are illustrative of the possible problems underlying bladder disorders and the sorts of avenues that could be explored within the mechanical framework. However, the model here presents just a first step in describing mathematically the complex environment within the bladder epithelium, and needs further development to be of practical clinical value. The focus in this study was entirely on the umbrella cell layer, though the epithelium also consists of basal and intermediate cell layers. These cell layers are not exposed to the lumen, and because of their limited number of intracellular vesicles their contribution to area modulation is likely to be negligible. Moreover, in terms of the capacitance measurements in refs. Yu et al. (2009), Truschel et al. (2002), these cell layers lack tight junctions, do not separate charge (during the transepithelial application of current), and as such they do not contribute to the changes in umbrella cell capacitance measured in the Ussing chamber. For these reasons, we opted to exclude them from our model. Nevertheless, these layers *do* affect the wall thickness and could alter the mechanical properties in a way that could modulate the responses of the epithelium to filling/stretch. However, this contribution is difficult to tease out as the umbrella cells cannot be studied experimentally in their absence. Incorporating a mechanical description of these layers and devising experimental approaches to isolate their effects remain as challenges for a future study.

There are a number of other interesting future directions, including incorporating more explicitly mechanosensing and the physical process of exo- and endocytosis. Due to the experimental accessibility of bladder epithelium, the former is particularly appealing, with a strong potential to better comprehend generic mechanotransduction pathways across molecular, cellular, and tissue levels. Finally, we have focussed on bladder filling in this paper, as this was the most relevant part of the bladder cycle that we could link with the experimental data. Equally important is to model voiding, at the cellular or vesicle level. However, this is not simply a reversal of the filling process. Rather, it requires a description of contraction of the surrounding detrusor muscle and endocytosis on a short time scale, which raises the issue of mechanical instability at the cell membrane and bladder tissue levels.

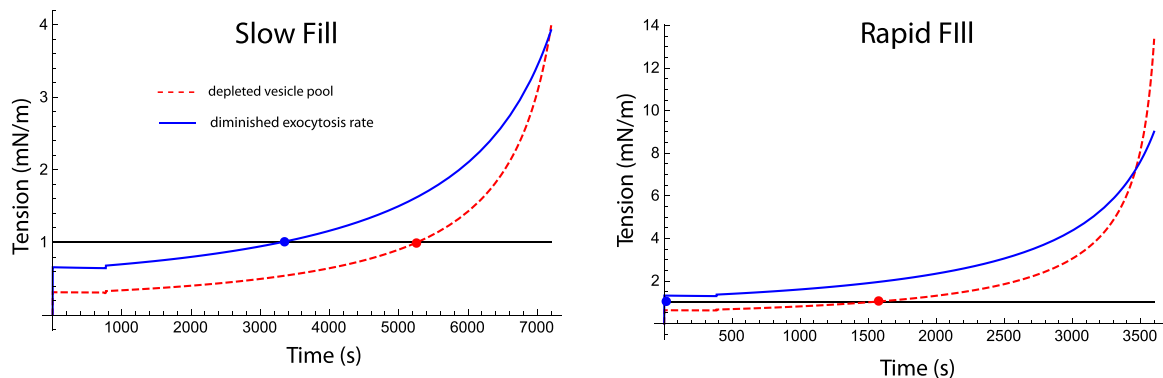


Fig. 10. Theoretical simulation for pathology discrimination. Tensions plotted for slow (0.03 mL/s) and rapid (0.06 mL/s) filling rates for two different pathologies: a depleted vesicle pool and a diminished (apical) exocytosis rate. The horizontal line represents a signalling threshold. The time at which the signalling threshold is crossed is indicated with the solid dots. Parameters are as in Tables in Appendix D, with \mathcal{A} changed to 311 cm^2 to model the depleted vesicle pool and k_{ad} changed to 12.5 for the diminished exocytosis.

Acknowledgements

This work was supported by National Institute of Diabetes and Digestive and Kidney Diseases Grants R37-DK-54425 and R01-DK-099196 to G.A and the Kidney Imaging Cores of the Pittsburgh Center for Kidney Research through Grant P30-DK-079307.

Appendix A. Model derivation

The mathematical model has four components: the fluid flow and pressure on both sides of the Ussing chamber, the geometry of the deforming disc of uroepithelial tissue, the mechanics of the apical and basal membranes of the umbrella cells, and the vesicle traffic that serves to dynamically change the reference membrane area. The equations governing each component are derived in turn below.

Poiseuille flow. We begin on the largest scale with a description of fluid flow in the Ussing chamber. Each hemichamber is connected to a cylindrical column of fluid with horizontal reserve, which feeds into the chamber. This geometry is depicted in Fig. A1 (a). Let Q_a be the apical flow rate, so that $Q_a > 0$ if fluid is entering the mucosal hemichamber, and equivalently define Q_b to be the

$$Q_a = -Q_b = \frac{d}{dt}V \quad (\text{A.3})$$

where V is the volume contained within the deforming spherical cap separating the two hemichambers. In other words, the change in volume in the spherical cap indicates how much fluid has entered the mucosal chamber, or equivalently has left the serosal hemichamber.

Cap geometry. We assume that at all times the bowed tissue may be approximated as a spherical cap.¹⁰ Considering first the apical membrane, and following the notation shown in Fig. A1(b), the radius of curvature r_a , surface area A_a and volume V_c depend on the midpoint deflection h_a and fixed radius d , via the following relations:

$$r_a = \frac{d^2 + h_a^2}{2h_a}, \quad (\text{A.4a})$$

$$A_a = \pi(h_a^2 + d^2) = 2\pi r_a h_a, \quad (\text{A.4b})$$

$$V = \frac{\pi h_a}{6}(h_a^2 + 3d^2). \quad (\text{A.4c})$$

The basal membrane is also assumed to be in a spherical cap

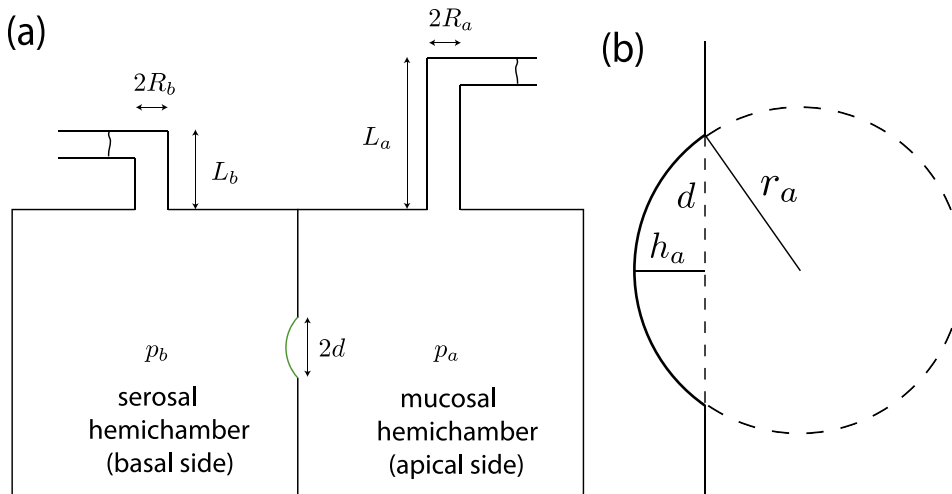


Fig. A1. (a) Ussing chamber geometry. (b) Cap geometry.

basal flow rate corresponding to the serosal hemichamber. The pressure at the top of the water columns remains fixed, due to the horizontal fluid reserve, at the values

$$P_a = \rho g L_a, \quad P_b = \rho g L_b, \quad (\text{A.1})$$

where ρ is the fluid density, g the gravitational constant, and $L_{a,b}$ are the vertical lengths of the columns of fluid. We assume that each hemichamber is at homogeneous pressure, which we denote $p_a(t)$ and $p_b(t)$ for the apical and basal sides, respectively. For each hemichamber, taking a Poiseuille flow through the two cylindrical tubes and enforcing constant flux, we obtain the relations

$$Q_a = \lambda_a(P_a - p_a), \quad Q_b = \lambda_b(P_b - p_b), \quad (\text{A.2})$$

where

$$\lambda_{a,b} = \frac{\pi R_{a,b}^4}{8\mu L_{a,b}}.$$

Here $R_{a,b}$ are the radii of tubing for each chamber, as shown in Fig. A1(a), and μ is the dynamic viscosity.

Mass conservation for an incompressible fluid implies that

geometry, with radius of curvature $r_b = r_a + \delta$, where δ is the (time varying) depth of the umbrella cells. The basal description also must take into account the morphological “unfolding” of the cells. That is, initially the basal side is curved and not supporting tension. As the tissue bows out, once a critical apical displacement h_a^* is reached, the cells have assumed a squamous shape and the basal membrane begins to support tension (see Fig. A2). The critical value h_a^* is computed in Appendix B. We denote the radius of curvature of the apical membrane at this point by r_a^* , and equivalently r_b^* for the basal membrane. Letting δ^* denote the cell depth at this point, we have $r_b^* = r_a^* + \delta^*$. As the tissue continues to bow outward, the two membranes form concentric spherical shells such that the intracellular volume, which we denote V_c , should remain approximately constant (Truschel et al., 2002). Computing V_c as the volume between two concentric spherical caps, and expanding in δ^* , we have

¹⁰ Initially the tissue is in a flat disc shape, which corresponds to a cap with infinite radius of curvature; however, for computational reasons we give a small non-zero radius at time zero.

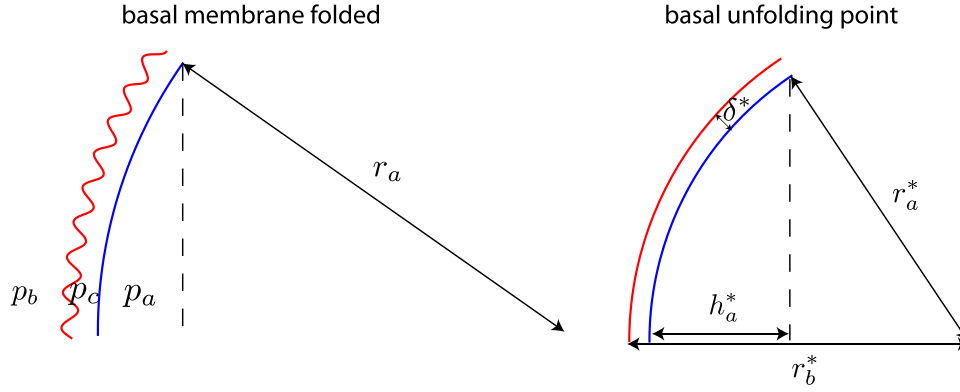


Fig. A2. Geometry of basal membrane and basal unfolding point.

$$V_c = 2\pi r_a^* h_a^* \delta^* + O(\delta^{*2}) \quad (\text{A.5})$$

where V_c is a fixed quantity determined by the cell geometry and tissue radius in the experimental setup. Beyond the unfolding point, we define the basal midpoint deflection and radius of curvature as h_b , r_b , respectively, with $h_b = h_a + \delta$, $r_b = r_a + \delta$; we can then approximate

$$2\pi r_a h_a \delta = 2\pi r_a^* h_a^* \delta^*, \quad (\text{A.6})$$

and thus

$$r_b = r_a + \frac{V_c}{2\pi r_a h_a}, \quad h_b = h_a + \frac{V_c}{2\pi r_a h_a}. \quad (\text{A.7})$$

Using (A.4b), along with (A.7), we note the basal surface area $A_b = 2\pi r_b h_b$ can be expressed in terms of h_a . In this way, $h_a = h_a(t)$ serves as the single geometric variable.

Membrane mechanics. In order to distinguish between activities at the basal versus the apical side of the umbrella cells, we consider each membrane mechanically as a thin elastic sheet that resists bending and stretching. However, as we now show, the bending energy in this setup is negligible compared to stretching energy. To see this, we assume a typical quadratic energy, so that the stretching energy of a piece of membrane with reference area A_0 that is stretched to area A is given by (see, e.g. Landau et al., 1986)

$$\mathcal{E}_s = \frac{1}{2}\mu \left(\frac{A}{A_0} - 1 \right)^2. \quad (\text{A.8})$$

where μ is the stretching modulus. The bending energy (per area) of an elastic sheet with radius of curvature R is

$$\mathcal{E}_b = \frac{1}{2}\kappa \frac{1}{R^2} \quad (\text{A.9})$$

where κ is the bending modulus, which scales as

$$\kappa \sim \mu \xi^2,$$

where ξ is the thickness of the membrane (Landau et al., 1986). To compare the relative size of the energies requires an estimation of the degree of stretching versus bending. We note that at its largest deflection, the area of the tissue in the experiments of Yu et al. (2009) is double the initial area, i.e. $A = 2A_0$ (the flat disc of tissue has bowed to a hemisphere). A stretch of 100% would far exceed the threshold for tissue rupture, hence the majority of this area increase must be accounted for by exocytosis, which will be described in the final component of the model. Taking as a modest value that only 1% is due to membrane stretching, we have

$$\mathcal{E}_s \approx 10^{-4}\mu.$$

As for bending, the thickness of a bilayer membrane is on the

order of 10 nm (Apodaca, 2003), but here there are two radii of curvature to consider. The radius of curvature of the bowed tissue (which starts out flat) during the Ussing experiments is bounded below by about 1 cm (the radius of the hemisphere), which yields $\mathcal{E}_b \approx 10^{-12}\mu$.

This suggests that in the apical membrane, bending energy is around 8 orders of magnitude smaller than stretching energy. The same will be true of the basal membrane beyond the unfolding point. Before the unfolding point, the basal membrane has a radius of curvature on the order of $10\mu\text{m}$, yielding a bending energy $\mathcal{E}_b \approx 10^{-6}\mu$, still 2 orders of magnitude smaller than stretching.¹¹

The above scaling arguments suggest that stretching effects dominate bending. With bending energy neglected, the membrane seeks to minimise surface area, subject to the imposed pressure difference across the two sides of the Ussing chamber. The pressure difference across each membrane is thus related to the in-plane membrane tension by a Young-Laplace-like law (Seifert, 1997)

$$\Delta p = \frac{2T}{R},$$

where Δp is the pressure difference across the membrane, T is the tension, and R is the radius of curvature. We denote the apical and basal tension by T_a and T_b , respectively. Recalling that p_a and p_b are the pressures in each hemichamber (see Fig. A1), and letting p_c be the intracellular pressure, we thus have

$$p_a - p_c = \frac{2T_a}{r_a}, \quad p_c - p_b = \frac{2T_b}{r_b}. \quad (\text{A.10})$$

Note that in the second equation, $T_b=0$ in the folded state, i.e. when $h_a < h_a^*$, and thus $p_c=p_b$ and the pressure difference is fully supported by the apical tension. Taking the sum of the two equations, we have

$$p_a - p_b = \frac{2T_a}{r_a} + \frac{2T_b}{r_b}. \quad (\text{A.11})$$

We can now combine the Young-Laplace relation and the flow rate to obtain an equation for the evolution of h_a . Combining Eqs. (A.2) and using Eq. (A.3), we have

$$\left(\frac{1}{\lambda_a} + \frac{1}{\lambda_b} \right) \frac{dV}{dt} = (P_a - P_b) - (p_a - p_b). \quad (\text{A.12})$$

Writing $dV/dt = V'(h_a) \frac{d}{dt} h_a$ and using (A.4c), (A.11), we then obtain

¹¹ Alternatively, we note the typical cited values for stretching modulus $\mu \approx 250\text{ mN/m}$ (Rawicz et al., 2000) and bending modulus $\kappa \approx 20k_B T$ (Lipowski and Sackmann, 1995). Then, at a 1% area stretch, stretching effects will dominate bending at a radius of curvature at or above $1\mu\text{m}$.

$$\frac{d}{dt}h_a(t) = \frac{2\lambda_a\lambda_b\left(\Delta P - 2\left(\frac{T_a}{r_a} + \frac{T_b}{r_b}\right)\right)}{\pi(\lambda_a + \lambda_b)(h_a^2 + d^2)}, \quad (\text{A.13})$$

where we denote $\Delta P := P_a - P_b$ as the imposed pressure difference.

Vesicle dynamics. As stated above, the roughly 100% increase in area requires significant exocytosis, i.e. membrane material must be added during the bowing to achieve such a large bowing without rupture. To model vesicle traffic, we assume that there is a fixed population of vesicles, with total combined surface area \mathcal{A} , and suppose that each vesicle will be in one of 4 states: (i) fused with apical wall, (ii) fused with basal wall, (iii) intracellular, (iv) being recycled. We define the proportion of the total vesicle population for each of the states as ϕ_a (State (i)), ϕ_b (State (ii)), ϕ_c (State (iii)), and ϕ_R (State (iv)), noting that each is a function of time and is restricted to lie between 0 and 1. The primary hypothesis we investigate in this study is that tension in the cell membranes drives exo- and endocytosis, in particular we propose that one or more of the following holds:

1. Tension in the apical membrane causes apical exocytosis;
2. Tension in the basal membrane causes basal exocytosis;
3. Tension in the apical membrane causes basal endocytosis;
4. Tension in the basal membrane causes apical endocytosis.

Moreover, we assume that vesicles fuse with either membrane from the intracellular population, and that endocytosed vesicles are not immediately available for exocytosis again, but rather undergo “recycling” and are only available for re-exocytosis after they have been reintroduced to the intracellular population. In particular, we propose that the vesicle dynamics can be described by

$$\begin{aligned} \frac{d}{dt}\phi_a &= \frac{k_{aa}}{\mu_a}\phi_c T_a - \frac{k_{ab}}{\mu_b}\phi_a T_b, \\ \frac{d}{dt}\phi_b &= \frac{k_{bb}}{\mu_b}\phi_c T_b - \frac{k_{ba}}{\mu_a}\phi_b T_a, \\ \frac{d}{dt}\phi_c &= k_R\phi_R - \phi_c\left(\frac{k_{aa}}{\mu_a}T_a + \frac{k_{bb}}{\mu_b}T_b\right), \\ \frac{d}{dt}\phi_R &= \frac{k_{ab}}{\mu_b}\phi_a T_b + \frac{k_{ba}}{\mu_b}\phi_b T_a - k_R\phi_R. \end{aligned} \quad (\text{A.14})$$

Here, the non-negative constants $k_{\alpha\beta}$ characterise the feedback between tension and vesicle traffic, and k_R is the rate at which vesicles are returned to the intracellular population. The constants $\mu_{a,b}$ characterize the membrane stiffnesses; these are included so that the $k_{\alpha\beta}$ have units of rates. The inclusion of the $\mu_{a,b}$ could be interpreted to mean that exo-, endocytosis are in fact being driven by stretch and not tension; however, as tension and stretch are linearly related such a distinction is not of consequence. The multiplying factors ϕ_α reflect the notion that exo- and endocytosis occur in rates in proportion to the amount of vesicle material, and ensures that each $\phi_\alpha \in [0, 1]$. Conservation of vesicles, i.e. $\phi_c + \phi_a + \phi_b + \phi_R = 1$, follows automatically from Eqn (A.14), which we can use to solve for ϕ_R and remove the final equation.

Membrane tension. The system (A.14) governs the time dynamics during deformation of the epithelial tissue. For given rate constants $k_{\alpha\beta}$, it remains to obtain expressions for the tensions T_a and T_b in terms of the vesicle populations and midpoint displacement h_a . To do so, we require a constitutive law relating the membrane stretch to tension. The quadratic stretching energy (A.8) yields a linear relation between the membrane tension and the areal stretch. Denoting $\alpha_{a,b}$ as the membrane stretch, we have

$$T_a = \mu_a(\alpha_a - 1), \quad T_b = \mu_b(\alpha_b - 1)H(h_a - h_a^*). \quad (\text{A.15})$$

The Heaviside function $H(h_a - h_a^*)$ accounts for the basal membrane supporting zero tension before the unfolding point. For each

membrane, the stretch is the ratio of geometric to reference (unstretched) area. As described above, the geometric area for both membranes can be written as a function only of h_a . The reference areas, which we denote $\hat{A}_a(t)$, $\hat{A}_b(t)$, will increase/decrease based on the amount of exo-, endocytosis, and will satisfy the following:

$$\hat{A}_a(t) = A_a(0) + \phi_a\mathcal{A}, \quad \hat{A}_b(t) = A_b^* + \phi_b\mathcal{A}. \quad (\text{A.16})$$

That is, the area of reference apical membrane at any time is equal to the initial amount plus whatever fraction ϕ_a of the total vesicle population \mathcal{A} is fused with the apical membrane, and similarly for the basal side. Here, A_b^* is the basal area at the point of basal unfolding, i.e. $A_b^* = 2\pi r_b^* h_b^*$, which is fixed by (A.7) once h_a^* is known. The stretches are then given by

$$\alpha_a = \frac{2\pi r_a h_a}{\hat{A}_a}, \quad \alpha_b = \frac{2\pi r_b h_b}{\hat{A}_b}, \quad (\text{A.17})$$

and we note that $\alpha_a = \alpha_a(h_a, \phi_a)$, $\alpha_b = \alpha_b(h_a, \phi_b)$.

Combining (A.13) and (A.14), and using (A.15)–(A.17), we obtain a closed system of 4 first order time-dependent ODEs for the variables $\{h_a, \phi_a, \phi_b, \phi_c\}$.

A.1. Full sphere model

We now adapt the model geometry from a spherical cap to a full sphere. In the case of a full sphere, the geometrical relations become simplified. The sphere radius (on the apical side) $r_a(t)$ forms the single geometric parameter, and the volume and area follow the familiar relations $V = 4\pi r_a^3/3$, $A_a = 4\pi r_a^2$. Assuming again that the intracellular volume remains constant, and expanding the volume between two concentric spheres in powers of the cell depth δ , we obtain

$$\delta = \frac{r_a^{*2}\delta^*}{r_a^2}, \quad (\text{A.18})$$

where δ^* and r_a^* are the depth and radius at the point of basal unfolding, as before. We can then write the basal radius $r_b = r_a + \delta$ in terms of r_a , and similarly for the basal geometric area A_b . We note that as well as basal unfolding, in vivo filling is first characterised by unfolding of the highly wrinkled apical membrane. In our model, we assume that the apical membrane is unfolded with zero tension at time $t=0$, i.e. we neglect any such small wavelength apical folds, which assumes that the majority of small folds are removed through mounting the tissue in a flat ring in the Ussing chamber, and is tantamount to considering the filling process starting at the unfolding point of the apical membrane.

As in the cap case, we posit 4 populations of vesicles, governed by (A.14). The tensions satisfy the constitutive relations

$$T_a = \mu_a(\alpha_a - 1), \quad T_b = \mu_b(\alpha_b - 1)H(r_a - r_a^*) \quad (\text{A.19})$$

where $\alpha_{a,b}$ are the areal stretches, that is

$$\alpha_{a,b} = \frac{4\pi r_{a,b}^2}{\hat{A}_{a,b}}, \quad (\text{A.20})$$

and the unstressed areas $\hat{A}_{a,b}$ follow (A.16). Since the geometric areas are both functions of r_a , the tensions are functions of $\{r_a, \phi_a, \phi_b\}$.

In completing the system, there are two distinct cases of interest: a pressure driven and volume driven system.

Pressure driven. To model pressure driven filling of a bladder, we suppose that a column of fluid of height L and radius R feeds into the bladder, thus creating an imposed pressure $P = \rho gL$. Taking Poiseuille flow into the bladder, the flux Q satisfies

$$Q = \frac{\pi R^4}{8\mu L}(P - p_a) \quad (\text{A.21})$$

where p_a is the intrabladder pressure, assumed uniform and equal to the pressure at the apical membrane. As before, we can equate the flux to the rate of change of bladder volume, which can in turn be expressed in terms of the radius, giving

$$Q = \frac{d}{dt}V = 4\pi r_a^2 \frac{d}{dt}r_a(t). \quad (\text{A.22})$$

The Young-Laplace relation applied across both the apical and basal membranes, and then combined, gives

$$p_a = \frac{2T_a}{r_a} + \frac{2T_b}{r_b}. \quad (\text{A.23})$$

Combining (A.21)–(A.23) gives

$$\frac{d}{dt}r_a(t) = \frac{R^4}{32\mu L r_a^2} \left(P - \frac{2T_a}{r_a} + \frac{2T_b}{r_b} \right). \quad (\text{A.24})$$

Volume driven. In the case of an imposed bladder volume, the system is simplified in that the geometry is predetermined and the pressure does not enter into the governing equations. We prescribe the bladder volume $V(t)$, in which case the radius is given by

$$r_a(t) = \left(\frac{3V}{4\pi} \right)^{1/3}.$$

Hence in this case the system consists of only three differential equations, for $\{\phi_a, \phi_b, \phi_c\}$.

Note that the difference between fixed volume and fixed pressure has a strong impact on the magnitude of the membrane tensions. In a pressure driven simulation, the apical membrane feels an ‘instantaneous’ imposed pressure, which creates a correspondingly large tension at $t=0$ following the Young-Laplace relation. Since the pressure difference is constant, the tension also stays at a relatively high value. In a volume driven simulation, on the other hand, it is natural to use initial conditions such that the membrane is at a baseline state (which for simplicity we assume is zero tension), after which the tension will increase in proportion with the rate of volume increase. With no fixed pressure, it is possible for the volume to be completely accommodated and the tension to return to its baseline state. Hence in the volume driven case we observe significantly lower magnitudes of tension.

Appendix B. Folding geometry

In the spherical cap geometry, r_a decreases as the apical chamber fills and the basal membrane unfolds. Here we use a geometric analysis to estimate the radius r_a^* at which the basal membrane becomes unfolded.

The geometry is illustrated in Fig. B1. Taking a cross section of the spherical cap model the basal membrane with a cosine curve, with each complete oscillation corresponding to a cell. Thus, with ω cells in the membrane, the frequency of the wave is

$$\hat{\omega} = \frac{\omega\pi}{\theta}, \quad (\text{B.1})$$

where

$$\theta = \arcsin\left(\frac{d}{r_a}\right) \quad (\text{B.2})$$

is the sector angle. Then, with amplitude ϵ , the radius of the basal side is

$$r = r_b + \epsilon \cos(\hat{\omega}\theta), \quad \theta \in [-\theta, \theta]. \quad (\text{B.3})$$

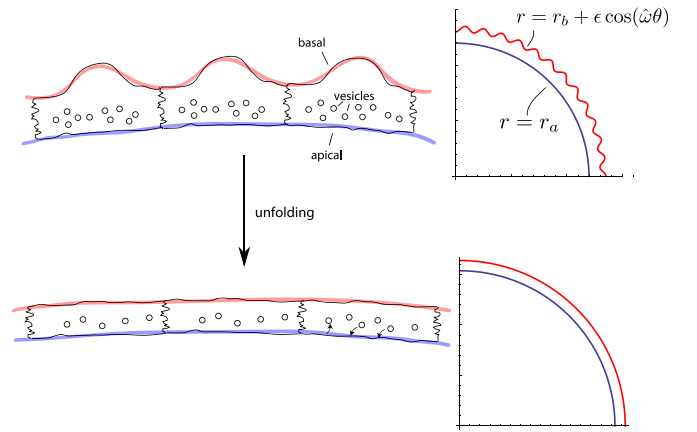


Fig. B1. Schematic for cell geometry and basal unfolding.

We assume that the length l_b of the basal membrane is constant prior to unfolding, since neither stretching nor vesicle trafficking occurs in the basal membrane while unfolding. We also assume, for simplicity, that the total area M between the apical and basal membranes remains fixed. In order to find r_a^* , the apical radius at the point of unfolding, we first need to find l_b and M , then let $\epsilon \rightarrow 0$ to simulate unfolding; $r_a^* = r_a(\epsilon = 0)$.

Initial cell dimensions were estimated from transmission and scanning electron micrographs of rabbit uroepithelia (Apodaca, 2003).

Here $\gamma(0)$ is the average initial width of a cell. Using these three values and taking a small non-zero initial value for h (to avoid an infinite radius of curvature), we can estimate the unfolding radius analytically. First, we use (A.4) and (B.2) respectively to find $r_a(0)$ and θ . Then $l_a(0)$ and $r_b(0)$ are given by

$$l_a(0) = 2\theta(0)r_a(0), \quad r_b(0) = r_a(0) + \delta(0), \quad (\text{B.4})$$

Finally, the number of cells ω is simply the initial apical length, $l_a(0)$, divided by $\gamma(0)$. We are now in a position to find the basal arclength and the intracellular area.

Arclength and area. Writing the basal curve in parametric form

$$(x, y) = r(\cos(\hat{\omega}\theta), \sin(\hat{\omega}\theta))$$

where r is given by (B.3), the arclength is

$$l_b = \int_{-\theta}^{\theta} \sqrt{x'^2 + y'^2} d\theta \quad (\text{B.5})$$

where ' denotes differentiation with respect to θ . Expanding for small ϵ we have

$$\sqrt{x'^2 + y'^2} = r_b + \epsilon \cos(\hat{\omega}\theta) + \epsilon^2 \frac{\hat{\omega}^2 \sin^2(\hat{\omega}\theta)}{2r_b} + O(\epsilon^3),$$

where $\hat{\omega}$ is given by (B.1), and so

$$l_b = \theta \left(2r_b + \frac{\epsilon^2 \hat{\omega}^2}{2r_b} \right) + 2 \frac{\epsilon}{\hat{\omega}} \sin(\hat{\omega}\theta) - \frac{\epsilon^2 \hat{\omega}}{4r_b} \sin(2\hat{\omega}\theta) + O(\epsilon^3). \quad (\text{B.6})$$

Thus we then find l_b , a constant, by plugging in the values θ , $r_b(0)$, $\epsilon(0)$ and $\hat{\omega}$ found above.

The total intracellular area M is given by

$$M = \int_{-\theta}^{\theta} \int_{r_a}^{r_b + \epsilon \cos(\hat{\omega}\theta)} r dr d\theta \quad (\text{B.7})$$

Table B1
Estimates of initial cell dimensions.

Dimension	Value (μm)
$\epsilon(0)$	5
$\delta(0)$	40
$\gamma(0)$	35

$$= \theta \left(r_b^2 + \frac{\epsilon^2}{2} - r_a^2 \right) + \frac{1}{\omega} \sin(\hat{\omega}\theta) \left(2r_b\epsilon + \frac{\epsilon^2}{2} \cos(\hat{\omega}\theta) \right). \quad (\text{B.8})$$

which again can be found by inserting the appropriate initial values.

Unfolding radius. In the spherical cap geometry, as ϵ decreases, r_b and r_a both decrease. Let $\epsilon \rightarrow 0$, then (B.6) becomes

$$l_b = 2r_b^* \theta^* = 2r_b^* \arcsin\left(\frac{d}{r_a^*}\right),$$

and so (B.8) becomes

$$M = \theta^* (r_b^{*2} - r_a^{*2}) = \arcsin\left(\frac{d}{r_a^*}\right) \left(\frac{l_b^2}{4\arcsin^2\left(\frac{d}{r_a^*}\right)} - r_a^{*2} \right). \quad (\text{B.9})$$

We solve (B.9) numerically, to find r_a^* given M and l_b ; there are multiple solutions, but we choose the solution that is greater than d , noting that $r_a = d$ is a hemisphere. The range in values of $\epsilon(0)$, from $3 \mu\text{m}$ to $5 \mu\text{m}$, gives a range in values of r_a^* from 1.36 cm to 0.94 cm . We have used a value of 1.11 cm in our simulations (Table B1).

Appendix C. Necessity of basal exocytosis

If no exocytosis occurs in the basal side, then $\phi_b = 0$ and the unstressed area A_b is fixed, with $A_b = A_b^* = 2\pi r_b^* h_b^*$. Now stretch in the basal membrane is given by $\alpha_b = \frac{2\pi r_b h_b}{A_b^*}$. From experimental data we see that the highest increase in capacitance is 112%, corresponding to the same percentage increase in the apical surface area. Thus

$$\max(2\pi r_a h_a) = 1.12 * (2\pi r_a(0) h_a(0)),$$

and with no exocytosis in the basal side we would have

$$\max(\alpha_b) = \frac{\max(2\pi r_b h_b)}{A_b} > \frac{\max(2\pi r_a h_a)}{A_b}.$$

With the parameters given in Appendix D, this gives at least a 61% stretch. However, it is known that uroepithelial cell membranes can only withstand 5–6% stretch, so basal exocytosis is clearly necessary to avoid rupture.

Appendix D. Model parameters

Model parameters for the spherical cap geometry are listed in Table D2, including a reference to how each parameter was determined. Most parameters can be estimated from the literature. Others require more consideration and are discussed further below.

Membrane stiffness. We first consider an estimation for the

Table D1
Sphere parameters.

Parameter	Description	Value
r_{a0}	Initial radius	3 mm
\mathcal{A}	Population of vesicles	356 cm^2
r_a^*	Unfolding radius	3.2 mm

membrane stiffness $\mu_{a,b}$ in the constitutive relation

$$T_{a,b} = \mu_{a,b}(\alpha_{a,b} - 1),$$

where $\alpha_{a,b}$ is the areal stretch. Areal stiffness estimates for red blood cell membranes can be found in the literature, but with a range of values that vary across several orders of magnitude (Skalak et al., 1973). Here, we use the turning point (the peak in the graphs of Fig. 1(b) in the main text) to estimate $\mu_{a,b}$. Geometrically, at this point the area has roughly doubled, meaning the cap should be close to a hemisphere, for which $r_a \approx r_b = d \approx 1 \text{ cm}$. At this point $\Delta P - \Delta p = 0$, which means that the imposed pressure difference ΔP is balanced by the tension in the membranes. Supposing that the tension in each membrane is of similar magnitude, $T_a \sim T_b$, we have from the Young-Laplace relation that $\Delta p \sim 4T_a/r_a$. At the largest pressure difference, $\Delta P = 15,680 \text{ g}\cdot\text{cm}^{-1}\cdot\text{s}^{-2}$, which gives a tension $T_a \approx 4000 \text{ g}\cdot\text{s}^{-2}$. Noting that the membrane will rupture at a stretch larger than about 6%, we have

$$4000 \approx T_a = \mu_a(\alpha - 1) \lesssim 0.06\mu_a,$$

from which we can estimate the stiffness $\mu_a \sim 6 \cdot 10^4 \text{ g}\cdot\text{s}^{-2}$, a value that is in the range cited for red blood cells. This value is an order of magnitude higher than values measured for phospholipid membranes via micropipette experiments (Tian et al., 2009). However, it is worth noting that our value is expected to be an overestimate, as the other cell layers in urothelial tissue (intermediate cells, e.g.) may be present in the experiments and will also support some of the tension, but are not explicitly included in the model. Also, since the apical membrane has a distinctly different makeup from the basal, there is no reason to assume that they should have the same mechanical properties. Our approach is to treat μ_a, μ_b as fitting parameters, both constrained to lie in the range $[10^3, 2 \cdot 10^5] \text{ g}\cdot\text{s}^{-2}$.

Further notes.

- To find the total vesicle area A , we use the result from Truschel et al. (2002) that for rabbit uroepithelia there is $8500 \mu\text{m}^2$ of vesicle surface area for $2700 \mu\text{m}^2$ of unstretched apical surface area. Hence

$$A = \frac{8500}{2700} * (2\pi r_a(0) h_a(0)), \quad (\text{D.1})$$

where $2\pi r_a(0) h_a(0) \approx \pi d^2$ is the initial apical surface area.

- The fluid used in the Ussing chamber is Krebs buffer solution, whose density ρ and viscosity μ we assume to be the same as water (i.e. the solution is sufficiently dilute).

Sphere model. For the full sphere model, vesicle trafficking rates and membrane stiffness are taken to be the same as in the cap model. Some geometrical parameters differ, and are listed in Table D1. In these values we have used the following calculations:

- $\mathcal{A} = \frac{8500}{2700} \cdot 4\pi r_{a0}^2$
- $r_a^* = \sqrt{1 + \left(\frac{h_a}{d}\right)^2} * r_{a0}$

Table D2

Model parameters for spherical cap.

Parameter	Description	Value	Reference
L_a	Apical column height	1–16 cm	(Yu et al. (2009))
L_b	Basal column height	0 cm	Authors' interpretation of Yu et al. (2009)
R_a	Apical column radius	0.2 cm	Yu et al. (2009)
R_b	Basal column radius	0.2 cm	Yu et al. (2009)
d	Opening radius	0.8 cm	Wang et al. (2003)
ρ	Fluid density	1 g/cm ³	Density of water
g	Gravitational acceleration	980 cm/s ²	Known value
μ	Fluid dynamic viscosity	$8.9 \cdot 10^{-3}$ g/cm/s	Viscosity of water
h_{a0}	Initial deflection	0.001 cm	Arbitrary small, non-zero value
\mathcal{A}	Population of vesicles	6.3 cm ²	Truschel et al. (2002)
δ^*	Unfolding cell thickness	0.001 cm	Order of magnitude estimate
k_{aa}	Apical exocytosis rate	30 s^{-1}	Fit to data
k_{bb}	Basal exocytosis rate	25 s^{-1}	Fit to data
k_{ab}	Apical endocytosis rate	30 s^{-1}	Fit to data
k_{ba}	Basal endocytosis rate	2.6 s^{-1}	Fit to data
k_R	Recycling rate	0.0038 s^{-1}	Fit to data
h_a^*	Unfolding deflection	0.34 cm	Determined geometrically
μ_a	Apical areal stiffness	140000 g/s ²	Fit to data
μ_b	Basal areal stiffness	70000 g/s ²	Fit to data

Appendix E. Data fitting and parameter estimation

The rate parameters $k_{\alpha\beta}$ and membrane stiffnesses $\mu_{a,b}$ were determined by fitting the model output to the ‘varying pressures’ experiment results in Fig. 5A of Yu et al. (2009). This represents a quantitative comparison with 5 different experimental runs, each with a different imposed pressure difference. For any given pressure, rate parameters can be chosen to match the data very well; here we use the values that minimise the total error over all 5 runs. As the model does not account for the slow and mild rise in surface area after reaching a plateau in Phase 3, the fit was made using data covering only the first five minutes.

Due to the multiple data sets and multiple parameters being fit simultaneously, the error function in a standard least squares approach contains many local minima. Hence it was necessary to obtain a good first guess for the initial parameters; this was done by

creating a Graphical User Interface allowing us to first fit the parameters by eye before performing a standard least squares curve fit.

We note also that the data for the initial increase in surface area, before the maximum is attained, is erratic: the lower pressure curves display an initial very small decrease in surface area; such a transient effect is not incorporated into our model, and created a mismatch at lower pressures that negatively affected the fit if considered. Hence only the points at and after the maximum were used for fitting, by artificially setting the noisy data for the initial rise and the corresponding outputs of the numerical solution to be zero.

Appendix F. Parameter sensitivity analysis

To investigate the robustness of the fit, as well as the effect of varying parameters on some important measures in the model, we

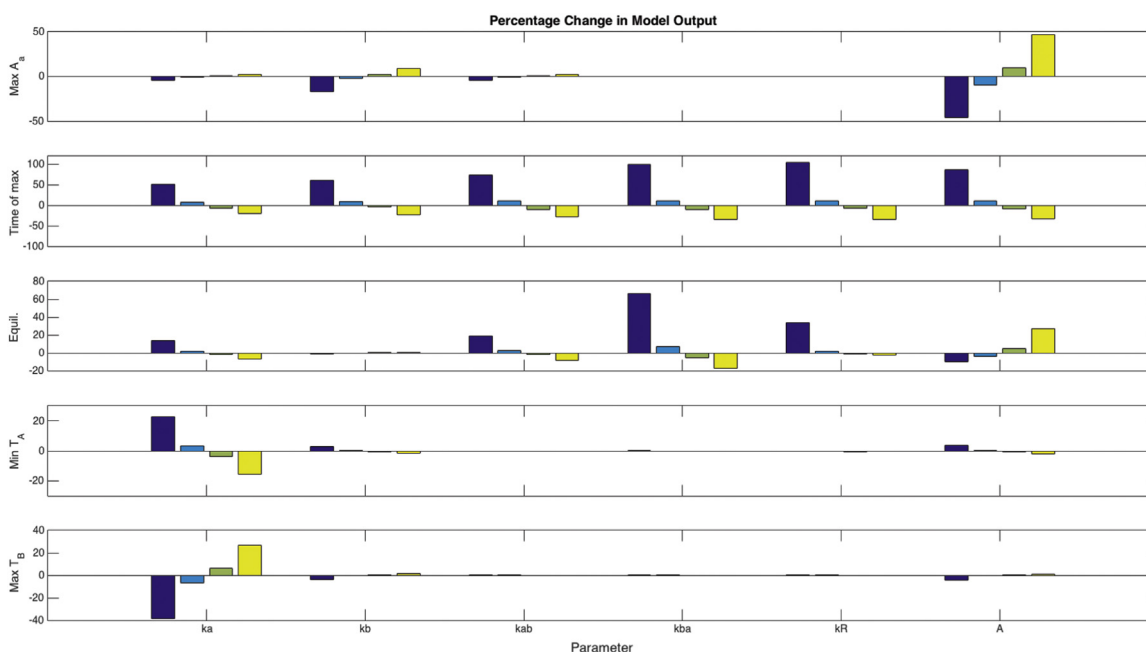


Fig. F1. Parameter sensitivity. Percent change in 5 model outputs for varying model parameters by 50% decrease (blue), 10% decrease (cyan), 10% increase (green), 50% increase (yellow). Model outputs: (i) maximum percentage increase in apical surface area (ii) time at which maximum area occurs (iii) equilibrium area percentage (iv) maximum basal tension, (v) apical tension when the basal tension is at a maximum. Model inputs: k_{aa} , k_{bb} , k_{ab} , k_{ba} , k_R , and the vesicle pool area \mathcal{A} . Base parameters as in Table D1.

performed a parameter sensitivity analysis of the fitted rate parameters (k_{aa} , k_{bb} , k_{ab} , k_{ba} and k_R) and the vesicle pool size \mathcal{A} one at a time. We increased and decreased each parameter individually by 10% and 50%, and measured the effect (percentage change from value with base parameters) on:

- The value of the maximum percentage increase in apical surface area.
- The time at which this maximum is reached.
- The equilibrium area percentage, approximated by the percentage increase in apical surface area after 5 min.
- The maximum basal tension.
- The apical tension when the basal tension is at a maximum.

We investigated the effect of changing each parameter individually on each of these measures for the 5 pressure differences in Yu et al. (2009), with $L_a = 1, 2, 4, 8$ and 16 cm. The output for $L_a = 2$ cm is provided in Fig. F1. The only feature for which the percent change in output is larger than the percent change in parameter input is the time at which maximum bowing occurs; however this largely reflects the fact that the maximum bowing occurs at a very short time.

Appendix G. Maximum bowing if no exocytosis

In this appendix we compute the maximum bowing that would occur in the spherical cap in the absence of exocytosis. We recall the relation

$$\frac{d}{dt}h_a(t) \propto (\Delta P - \Delta p),$$

which implies that bowing stops when $\Delta P = \Delta p$. We assume that in this case, the maximum bowing occurs before basal unfolding, an assumption that can be justified *a posteriori*. Before unfolding, the basal tension $T_b = 0$, and hence $\Delta p = 2T_a/r_a$. By combining the geometrical relation

$$r_a = \frac{d + h_a^2}{2h_a} \quad (\text{G.1})$$

with the constitutive relation (noting that with no exocytosis the unstressed area is fixed at $A_a(0)$)

$$T_a = \mu_a \left(\frac{2\pi r_a h_a}{A_a(0)} - 1 \right) \quad (\text{G.2})$$

we obtain the following equation

$$4\mu_a h_a \left(\frac{\pi}{A_a(0)} - \frac{1}{d^2 + h_a^2} \right) - \Delta P = 0, \quad (\text{G.3})$$

to be solved for the deflection h_a at the point of maximum bowing.

This cubic equation has a solution that for all pressures imposed is less than the unfolding deflection h_a^* . For example, with $L_a = 4$ cm, the maximum deflection occurs at $h_a \approx 0.14$ cm, which corresponds to an area increase of only 3%. Similar values are found for other pressures.

References

- Alroy, J., Weinstein, R.S., 1980. *Anat. Rec.* 197, 75–83.
- Apodaca, G., 2002. *Am. J. Physiol.-Ren. Physiol.* 282, F179–F190.
- Apodaca, G., 2003. *Traffic* 5, 117–128.
- Bastiaanssen, E.H.C., Van Leeuwen, J.L., Vanderschoot, J., Redert, P.A., 1996. *J. Theor. Biol.* 178, 113–133.
- Birder, L., De Groat, W., Mills, I., Morrison, J., Thor, K., Drake, M., 2009. *Neurorol. Urodyn.* 29, 128–139.
- Birder, L.A., Kanai, A.J., Cruz, F., Moore, K., Fry, C.H., 2010. *Neurorol. Urodyn.* 29, 598–602.
- Birder, L.A., Ruggieri, M., Takeda, M., van Koeveeringe, G., Veltkamp, S., Korstanje, C., Parsons, B., Fry, C.H., 2012. *Neurorol. Urodyn.*
- Brubaker, L., 2004. *Urology* 64, 12–16.
- Burnstock, G., 1999. *J. Anat.* 194, 335–342.
- Bykova, A.A., Regirer, S.A., 2005. *Fluid Dyn.* 40, 1–19.
- Carattino, M.D., Prakasam, H.S., Ruiz, W.G., Clayton, D.R., McGuire, M., Gallo, L.L., Apodaca, G., 2013. *AJP: Ren. Physiol.* 305, F1158–F1168.
- Colding-Jørgensen, M., Steven, K., 1993. *Neurorol. Urodyn.* 12, 59–79.
- Damaser, M.S., 1999. *Scand. J. Urol. Nephrol.* 33, 51–58.
- Damaser, M.S., Lehman, S.L., 1995. *J. Biomech.* 28, 725–732.
- Damaser, M.S., Lehman, S.L., 1996. *J. Biomech.* 29, 1615–1619.
- Fry, C.H., Sadananda, P., Wood, D.N., Thiruchelvam, N., Jabr, R.I., Clayton, R., 2011. *Neurorol. Urodyn.* 30, 692–699.
- Hildebran, J., Goerke, J., Clements, J., 1981. *J. Appl. Physiol.* 51, 905–910.
- Iggo, A., 1955. *J. Physiol.* 128, 593.
- Ingber, D.E., 2003. *Proc. Natl. Acad. Sci.*
- Khandelwal, P., Ruiz, W.G., Balestreire-Hawryluk, E., Weisz, O.A., Goldenring, J.R., Apodaca, G., 2008. *Proc. Natl. Acad. Sci. USA* 105, 15773–15778.
- Korossis, S., Bolland, F., Southgate, J., Ingham, E., Fisher, J., 2009. *Biomaterials* 30, 266–275.
- Korossis, S., Bolland, F., Ingham, E., Fisher, J., Kearney, J., Southgate, J., 2006. *Tissue Eng.* 12, 635–644.
- Landau, Lev D., and Lifshitz, E.M., *Course of Theoretical Physics 3* (1986): 109.
- Lewis, S.A., 2000. *Am. J. Physiol.-Ren. Physiol.* 278, F867–F874.
- Lewis, S.A., De Moura, J., 1984. *J. Membr. Biol.* 82, 123–136.
- Lewis, S.A., de Moura, J.L., 1982.
- Lipowski, R., and Sackmann, E., *Handbook of Biological Physics* (1995).
- Morris, C.E., Homann, U., 2001. *J. Membr. Biol.* 179, 79–102.
- Oliver, S., Fowler, C., Mundy, A., Craggs, M., 2002. *Neurorol. Urodyn.* 22, 7–16.
- Rawicz, W., et al., 2000. *Biophysical journal* 79 (1), 328–339.
- Sachs, F., Morris, C., 2015. *Mechanosensitive Ion Channels in Non Specialized Cells*. Springer, Berlin.
- Seifert, U., 1997. *Advances in Physics* 46 (1), 13–137.
- Skalak, R., Tozeren, A., Zarda, R.P., Chien, S., 1973. *Biophys. J.* 13, 245–280.
- Soldati, T., Schliwa, M., 2006. *Nat. Rev. Mol. Cell Biol.* 7, 897–908.
- Stahelin, L.A., Chlapowski, F.J., Bonneville, M.A., 1972. *J. Cell Biol.* 53, 73–91.
- Tian, A., Capraro, B.R., Esposito, C., Baumgart, T., 2009. *Biophys. J.* 97 (6), 1636–1646.
- Truschel, S.T., Wang, E., Ruiz, W.G., Leung, S.M., Rojas, R., Lavelle, J., Zeidel, M., Stoffer, D., Apodaca, G., 2002. *Mol. Biol. Cell* 13, 830–846.
- Wang, E., Truschel, S., Apodaca, G., 2003. *Methods* 30, 207–217.
- Wang, N., Naruse, K., Stamenovic, D., Fredberg, J.J., Mijailovich, S.M., Toric-Norrelykke, I.M., Polte, T., Mannix, R., Ingber, D.E., 2001. *Proc. Natl. Acad. Sci. USA* 98, 7765–7770.
- Yu, W., Khandelwal, P., Apodaca, G., 2009. *Mol. Biol. Cell* 20, 282–295.